POLITECNICO DI MILANO
LAUREA MAGISTRALE ING. AERONAUTICA
VON KARMAN INSTITUTE FOR FLUID DYNAMICS

NUMERICAL SIMULATION OF TWO-PHASE SOLID-LIQUID SLUSH FLOWS FOR PROPULSION SYSTEMS

RUBEN DI BATTISTA

Supervisor: Prof. Luciano Galfetti
Co-Supervisor: Prof. Maria Rosaria Vetrano (Von Karman Institute for Fluid Dynamics)
Co-Supervisor: Prof. Jean-Marie Buchlin (Von Karman Institute for Fluid Dynamics)

A mio padre, mia madre e mio fratello

$$\rho = |\tan \varphi|^{|\cot \varphi|}$$

Indice

Elenco delle figure

Elenco delle tabelle

Abstract

Slushes are two-phase solid-liquid single-species cryogenic fluids that exhibit an increased density and a greater heat capacity in respect to normal boiling point fluids. This promising features are of big interest for applications that exploit the slush as a thermal fluid, like super magnets refrigeration or air conditioning, and for aerospace systems that use slush fluids as fuel or oxidizer. Several programs in the frame of the research on Slush Hydrogen (SLH2) as a new-generation fuel for aerospace propulsion system have been started in the past and still continue to be performed in the present (National Aeronautics and Space Administration (NASA)'s National Space Plane (NASP), European Space Agency (ESA)'s Future European Space Transportation Investigations Programme (FESTIP) and Japan Aerospace eXploration Agency (JAXA) program for researh on SLH2 are the most famous examples).
In this work a numerical simulation based on a finite-volumes discretization using the software library OpenFOAM is carried on on solid-liquid multiphase flows (slurry) and slush flows inside a typical pipe geometry, very common in propulsion pipelines. A benchmark with previous experiments and simulations is also performed to assess the degree of accuracy of the code in predicting pressure drops and solid phase fraction dispersion. The effects of particle size, inlet velocity and concentration is also investigated.

Sommario

Gli «slush» sono correnti bifase solido-liquido composte da una singola specie in entrambi gli stati di aggregazione che esibiscono una densità più alta e una maggiore capacità termica rispetto al solo liquido puro. Queste promettenti caratteristiche sono di grande interesse in applicazioni che utilizzano gli slush come fluidi termici di lavoro, come per esempio nella refrigerazione dei super magneti, condizionamento e per sistemi aerospaziali dove gli slush andrebbero utilizzati come combustibili e/o ossidanti. Diversi programmi nell'ambito della ricerca sull'idrogeno slush (SLH2) sono stati inaugurati nel passato e continuano ad essere sviluppati nel presente (NASA's NASP, ESA's FESTIP e JAXA's program for research on SLH2 sono i pià famosi esempi). In questa tesi è presentata una simulazione numerica basata su una modellazione a volumi finiti (FVM) usando una la libreria opensource OpenFOAM di correnti bifase solido-liquido (cosiddetti «slurry flows») e correnti slush all'interno di una tipica geometria tubolare, molto comune nelle linee propulsive. Viene affrontata la validazione dei risultati su dati sperimentali provenienti da letteratura in modo da stimare il grado di accuratezza del codice nel predire le cadute di pressione e le distribuzioni di particolato solido. Vengono inoltre presentati gli effetti della dimensione delle particelle, della velocità di immissione e della concentrazione sulle caratteristiche della corrente.

Capitolo 1

Introduction

Solid-liquid two-phase flows have been investigated a lot during the years with practical applications in many sectors like the mining industry, the slurry pipelines that are used for transporting different types of slurries, the energy and conditioning engineering where different kind of slurries are currently investigated as replacement for the very polluting Chlorofluorocarbons (CFCs) in the refrigeration cycles, river mechanics, combustion efficiency in power generation plants, nuclear reactors operations, particle-accelerators cooling, etc...

Classically solid-liquid multiphase flows are addressed as a liquid carrier that drives inside of it a dispersed phase of particles with a well established concentration. Typical slurry pairs widely documented in the related literature are *water-sand*, *water-glass-beads* or *water-coal* that have been studied both in terms of experimental evaluation and numerical modeling.

Slush flows could be considered a particular type of solid-liquid multiphase flows defined by a liquid carrier of a particular fluid (interesting examples are Liquid Hydrogen (LH2), Liquid Nitrogen (LN2), Liquid Oxygen (LOX)) that drives inside of it a dispersed phase of particles of the *same* fluid in a different state of aggregation. This kind of flows are interesting because of their phase-changing nature that allows them to inherit better performances in terms of heat-transfer characteristics. Moreover the dispersion of particles inside the liquid carrier that exhibit higher density than the carrier allows to reach, for high concentration of solids, a higher overall density of the mixture. Such promising features are well suited to several applications like the already mentioned cooling cycle for air conditioning or super-magnets cooling. The increased overall density given by the higher-density dispersed particles and the improved heat transfer properties allowed by the phase change could be a game-changer aspect of the next generation space launchers and aerospace vehicles (e.g. scramjets).

The investigations on the use of SLH2 for aerospace application date back to the '60s in the frame of research on the NASP with the work of Sindt and collaborators [1]–[5]. Later on in the '80s and '90s the interest spread also to Europe with the ESA FESTIP program and in Japan with JAXA-contracted studies. SLH2 is a solid-liquid mixture of LH2 filled with solid particles of the same element that exhibits higher density and higher heat capacity (respectively +16.5% and +18% [1] or +15% and +18% [6]) in respect to the normal LH2 at the boiling point.
In Figure 1.1 the payload gain for an Earth-to-Orbit mission on a Shuttle is reported [6].

With the recent increase of private investment into space sector and the creation of highly innovative startups as SpaceX, the space industry is expected to move from government-only funded programs to highly competitive joint ventures between private and public stakeholders that would speed up

the development process of space technology. In such a frame of perspectives the adoption of new propulsion means is mandatory to achieve competitiveness and reliability. In facts SpaceX has recently used super-chilled oxygen as oxidizer of the new versions of Falcon 9 [7] with some minor troubles. This super-chilled oxygen could be seen as the step «just before» the adoption of slush oxygen.

In addition to the use of Slush Oxygen (SLO2) as oxidizer in a Liquid Rocket Engine (LRE), recently also the Hybrid Rocket Engines (HREs) have been rediscovered [8] in terms of performance and cost competitiveness against LREs and Solid Rocket Motors (SRMs). A configuration of a HRE for a lightweight space launcher (as planned by *Leaf Space s.r.l.*, an Italian startup that plans to develop *Primo*™, a HRE-powered nanolauncher) with SLO2 as oxidizer and wax as fuel surely deserves deeper study.

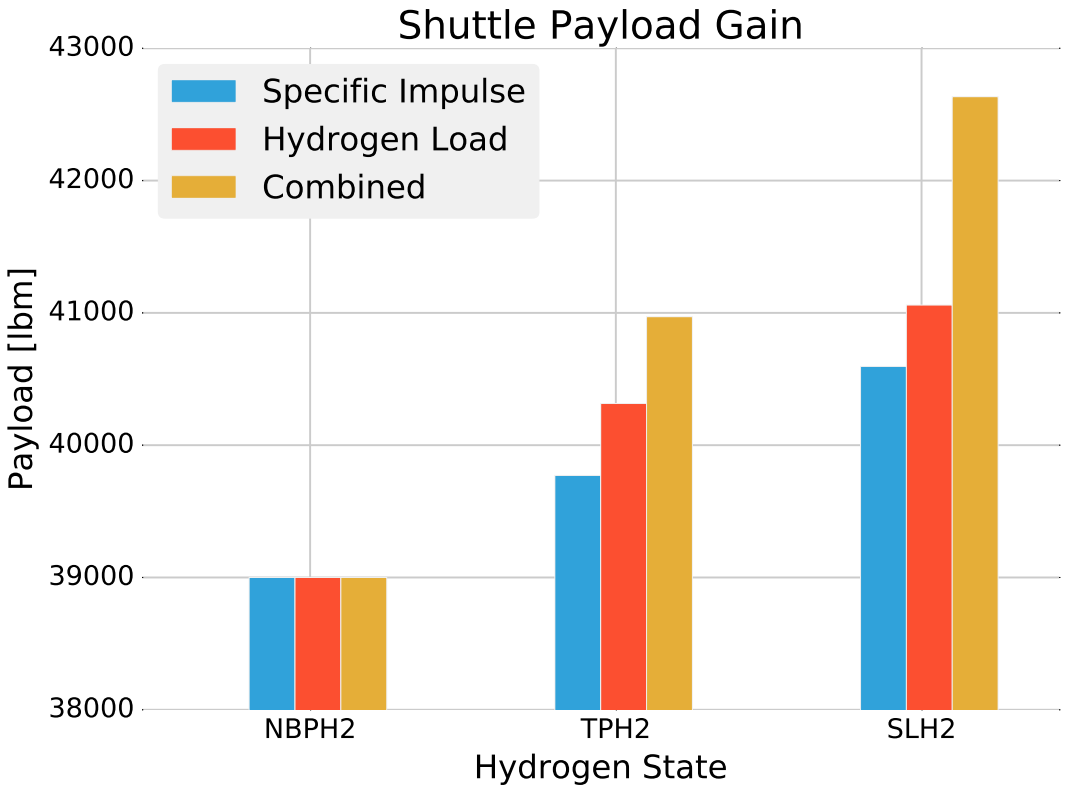

Figura 1.1: Shuttle payload gain when using different state of hydrogen [6]

1.1 Classification of slurries

Solid-liquid two-phase flows are reported in several different fields and applications, with several different working conditions spanning a wide plethora of physical situations. This deep intrinsic variance of scenarios made hard to establish a coherent and accepted classification of flow regimes. Moreover slush flows may (or may not) differ in behavior from the classical slurries even because the phenomenon is not fully understood.

Nonetheless a qualitative classification of flow regimes could be given based on the one already mentioned in [9, p. 4-52] in which four main type of flow regimes are identified: *homogeneous flow*, *heterogeneous flow*, *flow with a moving bed*, *flow with a stationary bed*.

Homogeneous flow

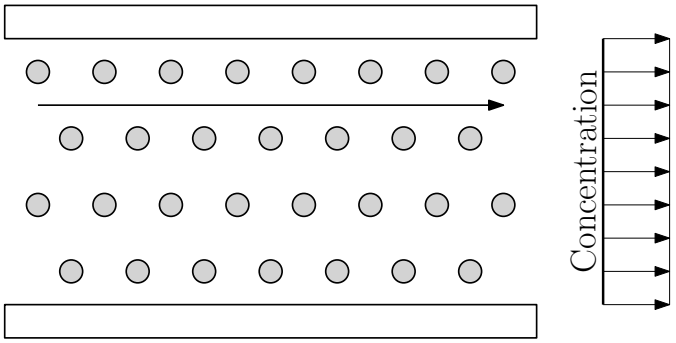

Figura 1.2: Homogeneous slurry flow

Homogeneous flow (Figure 1.2) is characterized by an homogeneous distribution of the solid particles along all the directions of the control volume. Generally this kind of slurries exhibit a newtonian viscous behavior. In some cases it is also possible to use a so-called *mixture model* that represents the multiphase compound as one equivalent fluid with average properties. This assumption easily allows the direct use of single-phase models and codes for the analysis of slurries even if it is sometimes hard to find reasonable correlations for some parameters limiting the applicability of those mixture models.

Heterogeneous flow

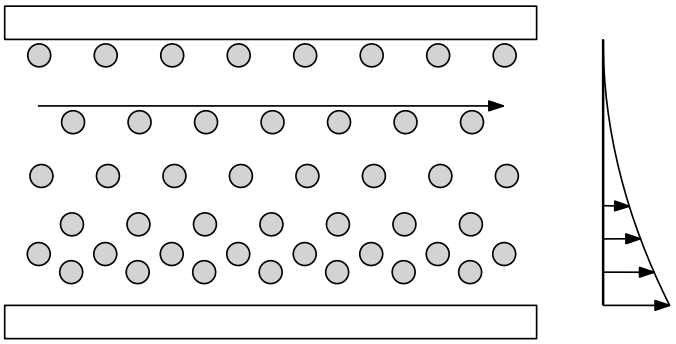

Figura 1.3: Heterogeneous slurry flow

Heterogeneous slurry flows (Figure 1.3) are probably the most common in industrial application, they're characterized by particles that are dense and big enough to start settling with various degrees leading to a concentratio that is not constant anymore along the cross-section and the length of the control volume. The majority of the particles, however, are still fully suspended in the carrier liquid.

The analysis of this kind of regime cannot exempt from a model that keep intact the different properties of the phases that have to be considered separately.

Moving bed flow

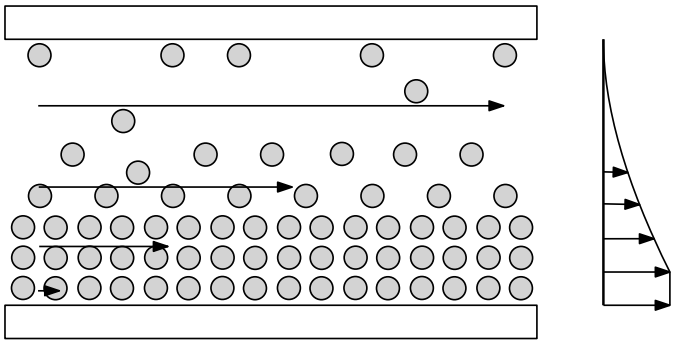

Figura 1.4: Moving Bed slurry flow

Moving Bed slurry flows (Figure 1.4) are observed when the larger and/or denser settling particles will accumulate on the bottom of the volume forming a bed and reaching the maximum packing limit. In the bed zone of the volume frictional stresses are high enough to make the particles move or slide along the length. The upper part of the volume, instead, is generally occupied by an heterogeneous slurry flow.

Stationary bed flow

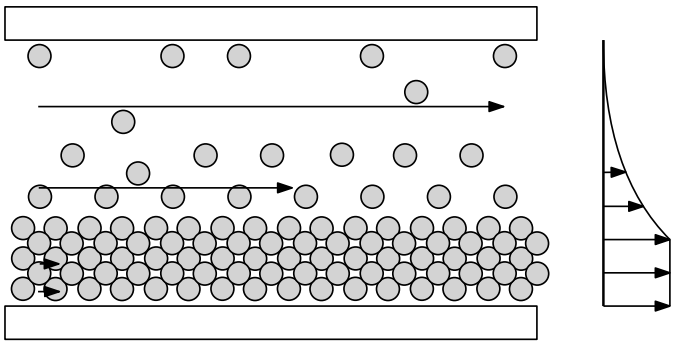

Figura 1.5: Stationary Bed slurry flow

Stationary bed slurry flows (Figure 1.5) are encountered when the velocity of the slurry is not high enough to carry all the particles that form a stationary bed at the bottom. This kind of regime, as suggested in [9, p. 4-53] has to be avoided since it gives unstable flow or, in the worst cases, plugging.

1.1.1 Stokes number

A more quantitative attempt to establish the flow regime is the definition of the *Stokes number* St, its definition and physical meaning can be derived considering the equation of motion for a single spherical particle in a fluid:

$$m\frac{\mathrm{d}\mathbf{u}_p}{\mathrm{d}t} = \frac{1}{2}C_D\frac{\pi d_p^2}{4}\rho_c\left(\mathbf{u}-\mathbf{u}_p\right)\left|\mathbf{u}-\mathbf{u}_p\right| \tag{1.1}$$

considering the Stokes result for the drag coefficient of a sphere for $Re \to 0$:

$$C_D = \frac{24}{Re} \tag{1.2}$$

and the definition of a Reynolds number for the particle:

$$Re_p = \frac{\rho_c D\left|\mathbf{u}-\mathbf{u}_p\right|}{\mu_c} = \frac{\rho_c D\left|\mathbf{u}_r\right|}{\mu_c} \tag{1.3}$$

the Equation (1.1) becomes:

$$\frac{\mathrm{d}\mathbf{u}_p}{\mathrm{d}t} = \frac{18\mu_c}{\rho_p d_p^2}\left(\mathbf{u}-\mathbf{u}_p\right) = \frac{1}{\tau_u}\left(\mathbf{u}-\mathbf{u}_p\right)$$

where the volume of a spherical particle has been considered for the mass $\left(m = \rho_p V = \frac{4}{3}\rho_p\pi\frac{d_p^3}{8}\right)$.

This way a *characteristic response time* of a particle associated to momentum exchange between the particle itself and the carrier fluid has been defined:

$$\tau_u = \frac{18\mu_c}{\rho_p d_p^2} \tag{1.4}$$

The Stokes number is defined as the ratio between the characteristic time of a particle τ_u and the characteristic time of the flow τ_f:

$$St = \frac{\tau_u}{\tau_f} = \frac{18\mu_c}{\rho_p d_p^2}\frac{U}{D} \tag{1.5}$$

Capitolo 2

State of the Art

In this chapter a literature survey about production, experimentation and modeling for cryogenic two-phase flows is provided. The interest will be mainly focused on SLH2 as it is one of the major candidates for the use in the new generation space launchers or space planes like the NASP or the concepts published in the frame of the ESA's FESTIP but the concepts are in general extendable to all the kind of slush flows used in several industrial and research applications like SLO2, Slush Nitrogen (SLN2) or Slurry Ice (SLH2O). A quite comprehensive research on literature about SLH2 is reported in [10] while another review on production and utilization of SLH2 is in [11]; the main findings in those papers are reported in this chapter with enrichments from other sources where needed.

2.1 Production Techniques

In the examined literature mainly two production techniques emerge: *Auger method* (Section 2.1.1) and *Freeze-thaw method* (Section 2.1.2) . Other methods are reported [10], [12] like *Helium injection* or *Magnetic Refrigeration* but there is not comparable documentation and they will not be described in this section.

2.1.1 Auger method

This metod is an alternative method to the one described in Section 2.1.2 that exploits the rotating movement of an auger that scrapes the solid layer of the fluid that froze on the cooled walls (since lower temperatures than hydrogen Triple-point (TP) are needed, gaseous or liquid helium are chosen as refrigerant). Differently from the method described in Section 2.1.2 the process is completely continous and not alternate. The process has been reported for the production of SLH2 [13]–[15] but also for SLO2 [15] and SLN2 [14], [16]. Problem with the auger locking, probably due to overcooling, is reported in [14]. In [15] the auger is also immersed in the liquid to be frozen. An image of a patent [17] describing a system for producing SLH2 with this method is showed in Figure 2.1.
In [15] the auger method for producing SLH2 is described in details. It's reported that, in spite of some irreversibilities associated to the extraction of the heat produced by the auger rotation, the systems seems to require less energy then the Freeze-thaw (F-T) method. A relation also for the power needed

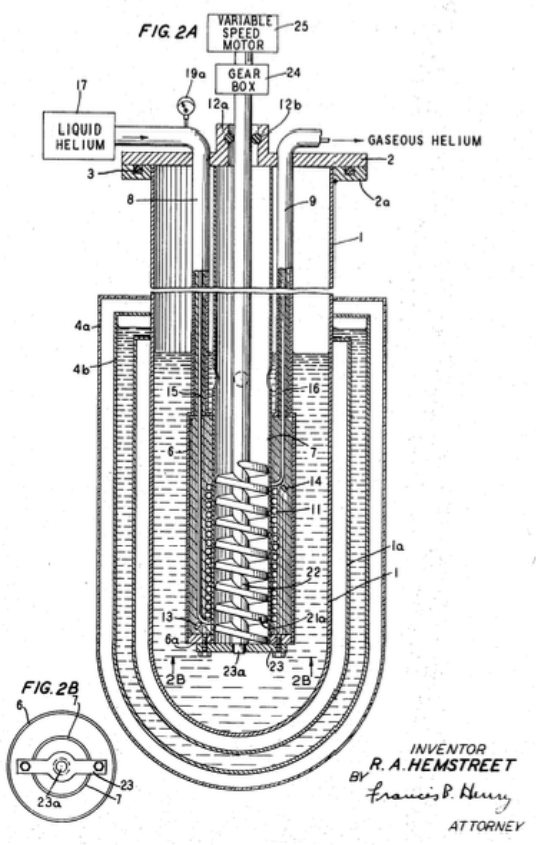

Figura 2.1: Image of auger method apparatus for producing SLH2 [17]

to produce slush with the auger method is suggested in Equation (2.1).
Size of particles reported is: $0.1-4$ mm [15]

$$\begin{aligned} P_d &= 0.0359\omega + 0.0014P_r \text{ For SLH2} \\ P_d &= 0.0359\omega + 0.0039P_r \text{ For SLO2} \end{aligned} \tag{2.1}$$

where ω is the rotational speed of the auger, P_d total power required to rotate the auger, P_r the refrigeration supplied to the auger assembly [W].

2.1.2 Freeze-thaw method

A method to produce SLH2 that exploits periodic vacuum pumping of the ullage over the LH2 creating solid layers on the surface. The pressure is lowered until the triple point of the LH2 (13.8K), a solid layer is hence produced. Following the production of the solid layer the pressure is allowed to increase and the solid layer just produced melts near the vessel walls and sinks into the liquid hence forming slush ([1], [13], [18]–[20]). A patent regarding this production methodology is showed in Figure 2.2.

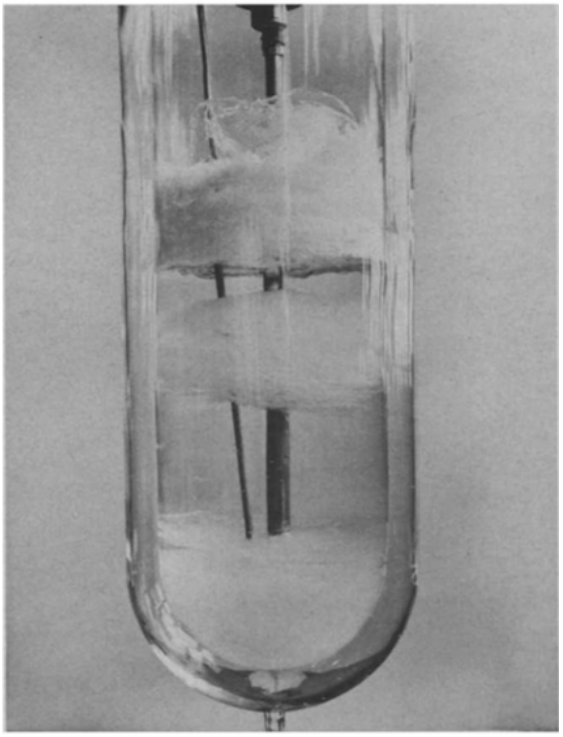

Figura 2.2: Image of freeze-thaw method for producing SLH2 [1]

An optimal rate of vacuum pumping is reported in [1] ($0.91\,m^3s^{-1}$ per $m^2$of surface area for vacuum pump inlet conditions of 300K and $6.9kN\,m^{-2}$) and in [18] a relation among the parameters influencing the production time is given by Equation (2.2). Other example of this production technique for slush nitrogen are reported in [21].

$$\frac{t_t}{t_{min}} = f\left(\frac{\Omega^{0.5} D_b^{0.75} D_g^{1.5} t_{th}^{0.5} L}{h^{0.5} V t_{fr}}\right) \tag{2.2}$$

The particle size reported in [15] for previous F-T methods measurements are in the range of $0.5-10$ mm with 2 mm being the mosto common size.

2.2 Experimental Setups

2.2.1 Density Measurements

Gamma Radiation attenuation

γ-rays attenuation method is proposed as density measurement techniques in [1], [22]. The measurement principle is based on the Lambert's Equation (Equation (2.3)):

$$I = I_0 e^{-\mu_M \rho\, l} \tag{2.3}$$

where I_0 and I are the ingoing and outgoing γ-ray flux, ρ is the density of the sample, l the lenght of the sample and μ_M the mass absorption coefficient. The μ_M coefficient is retrieved from XCOM database [23]. In [22] is reported that relative error on density is function of μ_M, l, and ρ itself Equation (2.4)

$$\frac{\Delta\rho}{\rho} = \frac{\Delta l}{l} + \frac{c'}{\sqrt{I_0}} \tag{2.4}$$

being:

$$c' = \frac{1 - \sqrt{e^{-\mu_M \rho\, l}}}{-\mu_M \rho\, l \sqrt{e^{-\mu_M \rho\, l}}}$$

Statistical error are reported for density measurements on different type of slushes and in particular for SLN2 an error of about 5.8% is highlighted.

Hydrostatic weighting

Capacitance and Waveguide Type

In [19], [24] densimeters based on capacitance changes are described. This kind of densimeter exploits the difference between the specific dielectric constant during the shift from liquid ($\varepsilon_l = 1.252$) to solid ($\varepsilon_s = 1.286$)to estimate SLH2 density. The dielectric constant - density relation is provided by the Clausius-Mossotti equation Equation (2.5) and the relation between capacitance and dielectric constant is given in Equation (2.6):

$$\frac{\varepsilon - 1}{\varepsilon + 2} = \rho P \tag{2.5}$$

$$C = C_0 \epsilon + C_d \tag{2.6}$$

When microwaves are transmitted through a medium whose dielectric constant is changing phase shift $\Delta\phi$ occurs. The phase shift is related to the dielectric constant change as showed in Equation (2.7):

$$\Delta\varepsilon = \frac{\lambda\sqrt{\varepsilon}}{180L}\Delta\phi \tag{2.7}$$

being λ the microwave wavelength, L the distance between receiving and transmitting antennas, ε the specific dielectric constant. Accuracy within ±0.5% is reported for the density measurement.

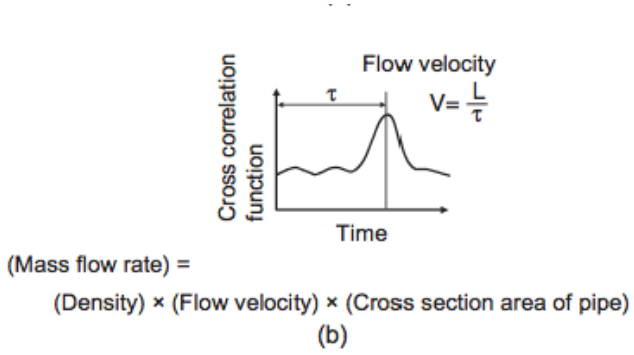

Figura 2.3: Working principle of the capacitance/waveguide flowmeter [19], [24]

2.2.2 Flow rate measurements

Capacitance and Waveguide Type

Using two waveguide type densimeters described in Section 2.2.1 installed in two different locations along the piped flow the flow velocity is calculated from the densimeters distance and the delay time when the cross-correlation functions of the two density signals was at maximum (see Figure 2.3) being V the velocity measured, L the distance of the densimeters and τ the delay time of the cross-correlation peak detection instant.

When using microwaves the variation in the said constant influences the cutoff frequency f_c by which the gain corresponding to the microwave transmission signal passing through the waveguide falls off like a step function as highlighted by the equation Equation (2.8):

$$f_c = \frac{c}{3.41a\sqrt{\varepsilon}} \tag{2.8}$$

The accuracy of the flowmeters is estimated to be «high enough» compared to the data achieved measuring the liquid level loss (±5%) but more experiments to confirm it are suggested.

2.2.3 Heat Transfer Measurements

Experiments and report on the heat transfer characteristics for SLH2 are somehow lacking in the literature; [2], [20] describe similar approaches to the study of the nucleate boiling heat transfer properties of triple point SLH2, triple point LH2 and even SLN2 and LN2: a circular flat plate of stainless steel of 0.025 m in diameter was used as the heat transfer surface for [2] while [20] uses an electrolytic tough pitch copper circular flat plate of the same size. The effect of the orientation angle ϕ of the heat transfer surface is also investigated.

The experimental setups described in [20] consists of three glass Dewar vessels nested together filled respectively, from the outer to the inner, of LN2, LH2 and SLH2. The purpose of the two most outer vessels is to lower the heat leak into the SLH2 from the outer environment. The experimental setup is showed in Figure 2.4.

The major outcomes of the experiments are:

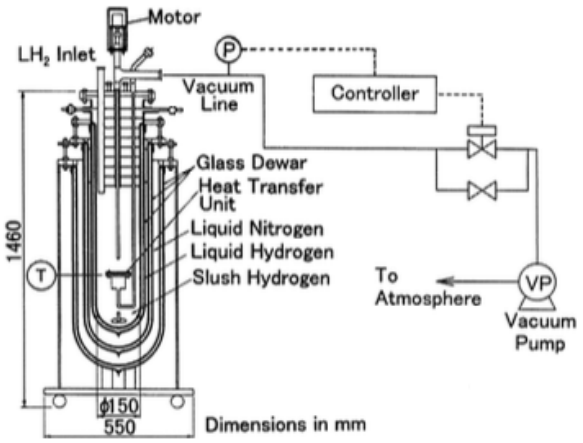

Figura 2.4: Experimental setup for heat transfer measurements [20]

- Heat transfer coefficient for SLH2 and SLN2 in the high-heat-flux region decrease up to 0.5 times those of LH2, LN2.
- Heat transfer coefficient for SLH2 in the low-heat-flux region slightly increase even in dependance of the heating surface orientation
- The Rosenhow equation Equation (2.9) (c_l: specific heat, μ_l: viscosity, ΔT: temperature difference at the heating surface, C_{sf}: factor dependant on the heat transfer surface material and liquid, σ: surface tension, λ: latent heat of vaporization) for predicting heat transfer coefficient is in accordance with SLN2 experiments but underestimation is reported for SLH2.

$$\frac{c_l \Delta T}{\lambda} = C_{sf} \left\{ \frac{q}{\mu_l \lambda} \left[\frac{\sigma}{g(\rho_l - \rho_v)} \right]^{\frac{1}{2}} \right\}^{0.33} Pr_l^s \tag{2.9}$$

In [12] silicon diode temperature sensors for temperature measurements are used to experimentally test the pressure drop and heat transfer coefficient drop for sln2.

The test setup provides 4 points of temperature sensing along the testing section of the 10mm and 15mm pipes. Critical velocities of about 2.0−3.0 m/s (14% SLN2) and over 3.6 m/s (10−30% SLN2) are reported in which a pressure drop decrease in respect of LN2 is confirmed.

2.0 m/s and 3.6 m/s respectively for 10 mm and 15 mm pipes are reported as critical velocity for heat transfer coefficient depression.

2.3 Handling

2.3.1 Piping

The handling of SLH2 is reported to be not very different from the LH2 up to 50% of solid fraction: the flow, in terms of hydraulics, behaves like the single-phase liquid. Transfer of SLH2 up to 60% of

solid fraction is reported inside of 16.6 mm up to 25 mm diameter pipes [1]. The minimum velocity that allows an homogeneous flow is reported to be 0.46 m/s for 16.6 mm diameter pipes.

In [25] a pipe of 15 mm is reported to be used for the grid and in [12], [26] pipes of 10 mm and 15 mm are used.

2.3.2 Heat leaks and pressure oscillations

Pressure oscillations are reported to arise [1], [10], [27] caused by thermal leak in SLH2. Basically the flow encounters a warmer environment and starts to vaporize; the pressure increases pushing it back to the source, even repeatedly. And in [1] a precooling of the pipes before letting the SLH2 flow in them is strongly advised.

2.3.3 Pressurization

The triple point conditions for SLH2 (0.08 bar at 13.8K), in particular the low pressure, could lead to higly dangerous security issues since air could leak into the tank and forming an easily-explosive mixture with the hydrogen itself. Moreover the low pressure inside the tanks could also cause structural problems (buckling). To overcome all this side effects pressurization with helium is reported in [1], [12], [13], [19], [24].

2.3.4 Aging

In [1] aging effects up to 100 hours are discussed. The aging phenomenon leads to an increase in settled slush density and in that paper it is explained as a result of heat leak into the slush. From a solid fraction of about $35-45\%$ for the freshly prepared slush after respectively 50 hours in a well insulated and shielded vessel ($\dot{Q} = 6.7 \cdot 10^{-8} \frac{\mathrm{W}}{\mathrm{cm}^3}$) and 17 hours in a vacuum insulated glass vessel with 20 times of heat imput a solid fraction of 60% is reached.

Capitolo 3

Numerical Modeling

Numerical simulation and Computational Fluid Dynamics (CFD) are tools that are gaining importance nowadays thanks to the quick increase of computational power density of modern, also commercial, processors. Often for multiphase flows, experimental sampling of some properties (i.e. velocity profiles and phase fractions) are very hard to accomplish also because of the operating conditions (i.e. low temperatures and pressures). In this frame of perspectives the possibility to predict complex fields thanks to the use of numerical analysis is very important for an efficient development of technological research.

In this chapter an overview of the mathematical models available for the simulation of slush and more generally slurry flows is discussed, with particular interest towards the Two-fluids model (2FM). Differences with the Lagrangian approach are briefly discussed and the Kinetic Theory for granular flows (KTGF) is also introduced.

3.1 Eulerian Two-Fluid Model

The considerations made in this section are focused to a system composed by two phases, a carrier liquid and a phase representing dispersed solid particles, but the Eulerian approach to multiphase modeling can be (and actually it is) extended also to systems that are characterized by several more phases that could behave as solids, liquids or gases.

In the Eulerian approach both the carrier phase and the particulate are modeled as interpenetrating continua characterized by Eulerian fields (like velocity $\mathbf{u}(\mathbf{x}, t)$) that are described by averaged conservation equations. The averaging process introduces the phase fraction α_φ which is defined as the probability that a certain phase is present at a certain point in space and time. Applying the Principle of Conservation of Difficulty[1] it is possible to understand how, even if several different regimes are possible to be simulated with the Eulerian approach, the difficulty migrates to the additional term that arises in the momentum conservation equation due to loss of information caused by the averaging process, named *interphase momentum exchange term*.

[1] Origin of this principle is somehow unknown. The author came into knowledge of it the first time when reported by Prof. Quartapelle in one of his Fluid Dynamics classes at *Politecnico di Milano*.

This chapter is dedicated to the formalization of the theoretical and numerical background of the work, a brief comparison against the Lagrangian approach is given in Section 3.1.1, comments about the averaging process are reported in Section 3.1.2 with particular focus on physical differences among time, volume and ensemble averaging, the governing equations are described in Section 3.1.4 and an overview on the KTGF that is used to model solid-fluid interactions is provided in Section 3.2.

Literature examples of use of this model on slush are not a lot, in [25], [28] an Finite Volume Method (FVM) Euler-Euler (E-E) approach is used to numerically model the problem. In [25] the choice is justified in order to minimize the computational cost. Other examples of numerical simulation performed in the frame of the Eulerian two-fluid model applied to slush flows are also [21], [29], [30]. In [31]–[33] the same theoretical and numerical background is applied to more classical slurries like sand-water, coal-water, glass-beads-water and ice slurry.

3.1.1 Differences with the Lagrangian Approach

The Euler-Lagrange (E-L) approach to two-phase modeling is to consider the liquid as a continuum, solving the Navier-Stokes (N-S) equations. The dispersed phase is solved by tracking a large number of particles and the conservation equations are expressed in a reference frame following the particle trajectory:

$$m_p \frac{\mathrm{d}\mathbf{u}_p}{\mathrm{d}t} = \sum \mathbf{F} \tag{3.1}$$

The expression of the several forces acting on the single particle $\mathbf{F}$ is not fully understood, an example of the most accepted form of the lagrangian equation for a particle is given in [34, Lagrangian Approaches].

Next to the apparent simplicity of the equation, another advantage of the Lagrangian approach is that, since one equation for each particle is needed, multiple particles are easily followable. In general the strategy for a Lagrangian approach is to follow a sufficient high number of particles, computing their trajectories, and then using that information to modify the flow field of the carrier (one-way coupling) retrieving all the necessary properties. This approach is applicable for multiphase flows with diluted dispersed phase (low phase fractions), otherwise a two-way coupling has to be implemented switching from the solution of the lagrangian equation to the eulerian equation of the carrier, than back to the particle problem until convergence is reached. Problem arise when expressing the initial conditions of the particles, since all the particles need to be equipped with an initial condition, that is often not knows. In that case a statistical Monte-Carlo approach is used. The biggest problems, however, are concentrated in the fact the the simulation of a large number of particles, which is always needed in industrial problems, is currently impossible due to the very high computational cost.

FVM with E-L approach are reported in [35], [36] even if the validation of the codes towards robust experimental data is somehow lacking or it is inadequate. In [30] a Finite Difference Method (FDM) is reported together with Lagrangian approach of particle tracking for SLN2 numerical investigation. In [37] an overview on the modeling for SLH2 flows is provided. In particular a limit for the maximum solid fraction that could be simulated in a E-L approach is evisaged to be $10-12\%$.

Since the slush meant to be used in propulsion should reach higher solid fractions up to 50%, an Eulerian approach in this particular case is preferred.

3.1.2 Averaging

The classical turbulence treatment is based on the averaging of the N-S equations using a time-average operator and the so-called «Reynolds decomposition» that represents a general fluctuating property as:

$$\mathbf{u}(\mathbf{x},t) = \overline{\mathbf{u}}(\mathbf{x}) + \mathbf{u}'(\mathbf{x},t) \tag{3.2}$$

where the first member in the Right Hand Side (RHS) represents a time averaged field,

$$\overline{\mathbf{u}}(\mathbf{x}) = \lim_{T\to\infty} \frac{1}{T} \int_0^T \mathbf{u}(\mathbf{x},t)\,\mathrm{d}t \tag{3.3}$$

and the last expression in the RHS is the fluctuating part of the field.

An alternative classical approach to the averaging process of the N-S equations is the volume averaging,

$$\overline{\mathbf{u}}(\mathbf{x},t) = \lim_{V\to\delta V} \frac{1}{V} \int_V \mathbf{u}(\mathbf{x},t)\,\mathrm{d}V \tag{3.4}$$

Both those approaches underlie constraints on the time/length scale that must be observed to keep the meaning of the resulting equations (i.e. when they are applied to multiphase flows care must be taken to account properly time/length scales of particles and turbulence) [34, p. 41].

In [34, p. 42] the ensemble averaging is reported to be the most mathematically rigorous since it allows to consider time and length scales that could be also infinitesimal and a wide explanation also on the number of averaging steps to accomplish is given. The final directives of that discussion are to use the ensemble average as the only averaging operator to be applied to the equations. In this frame of work, the phase fraction α has to be considered as the probability that a certain phase is present at a certain point in time and space.

Following the procedure reported in [34] and also employed in [38] , based on the work of [39], the conservation equations are derived *conditioning* the starting instantaneous microscopic equations with a *phase indicator function* so that contributions to the averaged conservation equations come only from regions (in space and time) that contain that particular phase. The phase indicator function is defined as

$$\chi_\varphi = \begin{cases} 1, & \text{If phase } \varphi \text{ is present} \\ 0, & \text{Otherwise} \end{cases} \tag{3.5}$$

3.1.3 Turbulence Modeling

The turbulence modeling of two-phase systems is a complex topic and the closure equations may vary in dependence with the specific problem (i.e. bubble flow, solid-liquid, liquid-gas, etc...).

Generally the fundamental assumption that is made for the closure of the momentum equation is to model the Reynolds stress using the so-called Boussinesq hypothesis

$$\mu_t = \rho C_\mu \frac{k^2}{\epsilon} \tag{3.6}$$

the Reynolds stress are computed as expressed in Equation (3.24) here below reported for convenience,

$$\mathbf{R} = -\rho\overline{\mathbf{u}'\mathbf{u}'} = \mu_t\left(\nabla\overline{\mathbf{u}} + \nabla\overline{\mathbf{u}}^T\right) - \frac{2}{3}\rho k\mathbf{I} \tag{3.7}$$

while the turbulent kinetic energy and the turbulent dissipation rate behavior is described by two transport equations:

$$\frac{\partial \rho\alpha\epsilon}{\partial t} + \nabla\cdot(\rho\alpha\epsilon\overline{\mathbf{u}}) = \nabla\cdot\left[\alpha\left(\mu + \frac{\mu_t}{\sigma_\epsilon}\right)\nabla\epsilon\right] + C_1\rho\alpha G\frac{\epsilon}{k} - C_2\rho\alpha\frac{\epsilon}{k} + \rho\alpha\Pi_\epsilon \tag{3.8}$$

$$\frac{\partial \rho\alpha k}{\partial t} + \nabla\cdot(\rho\alpha k\overline{\mathbf{u}}) = \nabla\cdot\left[\alpha\left(\mu + \frac{\mu_t}{\sigma_k}\right)\nabla k\right] + \rho\alpha G - \rho\alpha\epsilon + \rho\alpha\Pi_k \tag{3.9}$$

where in general $C_\mu = 0.09$, $C_1 = 1.44$, $C2 = 1.92$, $\sigma_k = 1$, $\sigma_\epsilon = 1.3$ and G is given by Equation (3.10).

$$G = \mu_t\left(\nabla\overline{\mathbf{u}} + \nabla\overline{\mathbf{u}}^T\right) \tag{3.10}$$

The source terms Π_k, Π_ϵ can be expressed in rapport to the specific problem, for example addressing for bubble-generated or particle-generated turbulence. More details on multiphase turbulence modeling can be more deeply investigated reading [40].

3.1.4 Governing Equations

Mass Conservation

An example of the application of the *conditioning* process briefly described in Section 3.1.2 is here applied to the mass conservation equation (from [34]). Starting from the local mass balance equation

$$\frac{\partial \rho}{\partial t} + \nabla\cdot(\rho\mathbf{u}) = 0 \tag{3.11}$$

phase conditioning is applied ad then the ensemble averaging is performed resulting in

$$\overline{\chi_\varphi\frac{\partial \rho}{\partial t}} + \overline{\chi_\varphi\nabla\cdot(\rho\mathbf{u})} = 0 \tag{3.12}$$

that can be rearranged to give

$$\frac{\partial \overline{\chi_\varphi \rho}}{\partial t} + \nabla \cdot \overline{\left(\chi_\varphi \rho \mathbf{u}\right)} = \overline{\rho \frac{\partial \chi_\varphi}{\partial t}} + \overline{\rho \mathbf{u} \cdot \nabla \chi_\varphi} \tag{3.13}$$

The derivative of the phase indicator can be linked to the motion of the interface between phases [34, Appendix A]

$$\frac{\partial \chi_\varphi}{\partial t} = -\mathbf{v_i} \cdot \nabla \chi_\varphi \tag{3.14}$$

so the equation becomes

$$\frac{\partial \overline{\chi_\varphi \rho}}{\partial t} + \nabla \cdot \overline{\left(\chi_\varphi \rho \mathbf{u}\right)} = \overline{\rho \left(\mathbf{u} - \mathbf{v}_i\right) \cdot \nabla \chi_\varphi} \tag{3.15}$$

The conditional averaged quantities (i.e. the quantities related to one specific phase φ are expressed as

$$\overline{\gamma_\varphi} = \frac{\overline{\chi_\varphi \gamma}}{\alpha_\varphi} \tag{3.16}$$

being γ a generic property (e.g. density ρ) and α_φ the phase fraction. This allows to write the Equation (3.15) as

$$\frac{\partial \alpha_\varphi \overline{\rho}_\varphi}{\partial t} + \nabla \cdot \left(\alpha_\varphi \overline{\rho_\varphi \mathbf{u}_\varphi}\right) = \left\langle \rho_\varphi \left(\mathbf{u}_\varphi - \mathbf{v}_i\right) \cdot \mathbf{n} \right\rangle_i \Sigma \tag{3.17}$$

where the notation $\langle \gamma \rangle \Sigma$ is defined as the surface integral per unit volume divided by the surface area per unit volume Σ [34, Appendix A],

$$\langle \gamma \rangle = \frac{1}{\Sigma} \lim_{\delta V \to 0} \overline{\frac{1}{\delta V} \int_{\delta S} \gamma \, \mathrm{d}S} \tag{3.18}$$

where

$$\Sigma = \lim_{\delta V \to 0} \overline{\frac{1}{\delta V} \int_{\delta S} \mathrm{d}S} \tag{3.19}$$

This can be interpreted as the surface-weighted value of γ at the interface.

The last term of the RHS of Equation (3.17) is null for non-reacting interfaces (since the velocity of the interface $\mathbf{v}_i$ is equal to the velocity of the phase φ at the interface). Hence the equation can be simplified as:

$$\frac{\partial \alpha_\varphi \overline{\rho}_\varphi}{\partial t} + \nabla \cdot \left(\alpha_\varphi \overline{\rho_\varphi \mathbf{u}_\varphi}\right) = 0 \tag{3.20}$$

Momentum conservation

Applying the same concepts of phase-conditioning and ensemble averaging an averaged version of the momentum conservation can be derived:

$$\frac{\partial \alpha_\varphi \rho_\varphi \overline{\mathbf{u}}_\varphi}{\partial t} + \nabla \cdot \left(\alpha_\varphi \rho_\varphi \overline{\mathbf{u}}_\varphi \overline{\mathbf{u}}_\varphi\right) + \nabla \cdot \left(\alpha_\varphi \overline{\mathbf{R}}_\varphi^{\text{eff}}\right) = -\alpha_\varphi \nabla \overline{p} + \alpha_\varphi \rho_\varphi \mathbf{g} + \overline{\mathbf{M}}_\varphi \tag{3.21}$$

where $\overline{\mathbf{R}}_\varphi^{\text{eff}}$ is the combined turbulent and viscous stress

$$\overline{\mathbf{R}}^{\text{eff}} = \overline{\boldsymbol{\tau}}_f + \overline{\mathbf{R}} \tag{3.22}$$

being (with the hypothesis of incompressibility $\nabla \cdot \overline{\mathbf{u}} = 0$)

$$\boldsymbol{\tau}_f = \mu\left(\nabla \overline{\mathbf{u}} + \nabla \overline{\mathbf{u}}^T\right) \tag{3.23}$$

and

$$\mathbf{R} = -\rho \overline{\mathbf{u}'\mathbf{u}'} = \mu_t \left(\nabla \overline{\mathbf{u}} + \nabla \overline{\mathbf{u}}^T\right) - \frac{2}{3}\rho k \mathbf{I} \tag{3.24}$$

hence

$$\overline{\mathbf{R}}^{\text{eff}} = (\mu + \mu_t)\left(\nabla \overline{\mathbf{u}} + \nabla \overline{\mathbf{u}}^T\right) - \frac{2}{3}\rho k \mathbf{I} \tag{3.25}$$

and $\overline{\mathbf{M}}_\varphi$ is the interphase momentum exchange term.

3.1.5 Interphase Momentum Exchange

In the averaged momentum equation (Equation (3.21)) there is a term of each phase φ that embodies the exchange of momentum between them. It needs modeling.

First of all, since also the total momentum over all the phases is conserved, the sum of all the interphase momentum exchange terms has to be zero

$$\sum_\varphi \overline{\mathbf{M}}_\varphi = 0 \tag{3.26}$$

Moreover, restricting the considerations on multiphase flows composed by two different phases, only one expression it is needed to close the system of equations. As reported in [38], the term is derived considering all the forces acting on the single particle. The most important are: *drag*, *lift*, *virtual mass*, while other forces can be added as the Soret effect (also knows as *termophoresis* for liquid mixtures, i.e. the generation of a force caused by a strong temperature gradient, it is the symmetric effect of the Dufour effect) or turbulent dispersion (i.e. generation of a drag-like term due to turbulence and equation averaging).

	Standard	Phase Inversion
$\overline{\mathbf{M}}_a^{\text{drag}}$	$\alpha_a \frac{3}{4} \frac{\rho_b}{d_a} C_D \lvert\overline{\mathbf{u}}_r\rvert \overline{\mathbf{u}}_r$	$\alpha_a \alpha_b \frac{3}{4} \left(f_a \frac{C_{D_a} \rho_b}{d_b} + f_b \frac{C_{D_b} \rho_a}{d_a} \right) \lvert\overline{\mathbf{u}}_r\rvert \overline{\mathbf{u}}_r$
$\overline{\mathbf{M}}_a^{\text{lift}}$	$\alpha_a C_L \rho_b \overline{\mathbf{u}}_r \times (\nabla \times \overline{\mathbf{u}}_b)$	$\alpha_a \alpha_b f_a \left(C_{L_a} \rho_b \overline{\mathbf{u}}_r \times (\nabla \times \overline{\mathbf{u}}_a) \right) + \alpha_a \alpha_b f_b \left(C_{L_b} \rho_a \overline{\mathbf{u}}_r \times (\nabla \times \overline{\mathbf{u}}_b) \right)$
$\overline{\mathbf{M}}_a^{\text{v.m.}}$	$\alpha_a C_{\text{v.m.}} \rho_b \left(\frac{D_b \overline{\mathbf{u}}_b}{Dt} - \frac{D_a \overline{\mathbf{u}}_a}{Dt} \right)$	$\alpha_a \alpha_b \left(f_a C_{\text{v.m.}_a} \rho_b + f_b C_{\text{v.m.}_b} \rho_a \right) \left(\frac{D_b \overline{\mathbf{u}}_b}{Dt} \frac{D_a \overline{\mathbf{u}}_a}{Dt} \right)$

a, b are two generical phases. b is the continuous phase. d_a is the diameter of the dispersed phase. f_a and f_b are blending functions such that $\alpha_\varphi \to 0, f_\varphi \to 0$
$\frac{D_\varphi \phi}{Dt} = \frac{\partial \phi}{\partial t} + \overline{\mathbf{u}}_\varphi \cdot \nabla$

Tabella 3.1: Interface momentum exchange terms

$$\overline{\mathbf{M}}_\varphi = \overline{\mathbf{M}}_\varphi^{\text{drag}} + \overline{\mathbf{M}}_\varphi^{\text{lift}} + \overline{\mathbf{M}}_\varphi^{\text{v.m.}} + \overline{\mathbf{M}}_\varphi^{\text{oth.}} \tag{3.27}$$

The form of the various terms is reported in Table 3.1, also including forms that account for phase inversion (i.e. zones of the domain where the continuous phase becomes dispersed $\alpha_b \to 0$).

3.1.5.1 Drag

In the large number of interphase forces acting between the two phases, surely the drag force is the most important and the one that is always accounted for in all the slurry and slush simulations, both for Lagrangian and Eulerian approaches, (e.g. [21], [30], [35], [40]).

Generically the drag is modeled considering the disperse system as composed by spherical particles. Several models for the correlation of the drag coefficient of spheres in different regimes of *Re* have been proposed during the years, some that could be extended to a generical Discrete Particle Element (DPE) (i.e. a bubble, a droplet or a solid particle), other more specialized and focused to specific application. A representative image of the drag coefficient profile for a sphere at different *Re* is showed in Figure 3.1

For the granular flows several interphase drag exchange correlations are available specifically coined for the problem under examination. The most popular in the recent literature are the *Syamlal O'Brien* model and the *Gidaspow* model that it is an hybrid model that applies the *Ergun* model or the *WenYu* model on the base of the particle Reynolds number Re_p and phase fraction of the solid α_a. Very good comparisons of drag models for granular models are reported in [41], [42]. Another good reference is the ANSYS FLUENT Theory Guide. The two models predictions of the C_D are showed in Figure 3.2

$$Re_p = \frac{\rho_c D \lvert\mathbf{u}_r\rvert}{\mu_c}$$

Syamlal O'Brien
The Syamlal O'Brien model is derived for a singular spherical particle. The C_D reported in the standard interphase drag exchange term reported in Section 3.1.5 is redefined in terms of a *relative velocity* V_r that is than given by a correlation:

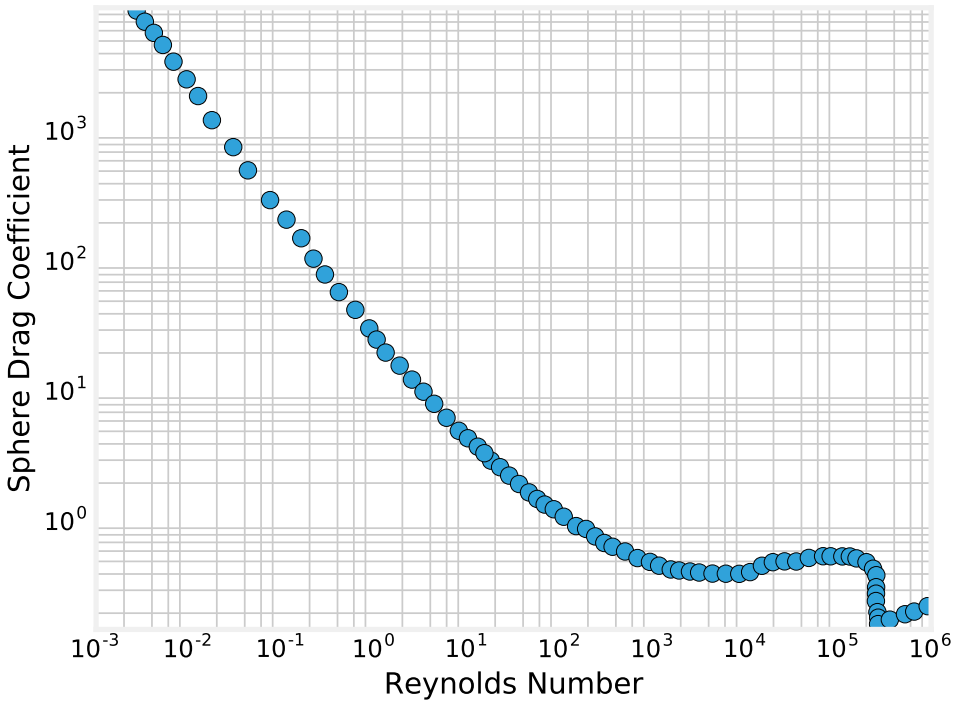

Figura 3.1: Sphere drag coefficient at different regimes

$$C_D = \widetilde{C_D}\frac{(1-\alpha_a)}{V_r^2} \tag{3.28}$$

$$\widetilde{C_D} = \left(0.63 + 4.8\sqrt{\frac{V_r}{Re_p}}\right) \tag{3.29}$$

$$V_r = \frac{1}{2}\left(A - 0.06Re_p\right) + \sqrt{\left(0.06Re_p\right)^2 + 0.12Re_p\left(2B - A\right) + A^2} \tag{3.30}$$

$$A = (1-\alpha_a)^{4.14} \tag{3.31}$$

$$B = \begin{cases} 0.8\,(1-\alpha_a)^{1.28} & \text{if } \alpha_a \geq 0.15 \\ (1-\alpha_a)^{1.28} & \text{if } \alpha_a < 0.15 \end{cases} \tag{3.32}$$

Gidaspow
The Gidaspow model applies the Ergun model for higher solid fractions and the WenYu model otherwise:

$$C_D = \begin{cases} \widetilde{C_D}\,(1-\alpha_a)^{-1.65} & \text{if } \alpha_a \leq 0.2 \\ \frac{200\alpha_a\mu_b}{(1-\alpha_a)d_a\rho_b|\mathbf{u}_r|} + \frac{7}{3} & \text{if } \alpha_a > 0.2 \end{cases} \tag{3.33}$$

the expression for the C_D in case of $\alpha_a > 0.2$ is derived from the original expression that is written in terms of the interphase exchange term:

$$\overline{\mathbf{M}}_a^{\text{drag}} = 150\frac{\alpha_a^2\mu_b}{(1-\alpha_a)\,d_a^2} + \alpha_a\frac{7}{4}\frac{\rho_b}{d_a}\,|\mathbf{u}_r| \tag{3.34}$$

The drag coefficient is given by:

$$\widetilde{C_D} = \begin{cases} \frac{24}{Re_p(1-\alpha_a)}\left[1 + 0.15\left((1-\alpha_a)Re_p\right)^{0.687}\right] & \text{if } (1-\alpha_a)Re_p < 1000 \\ 0.44 & \text{if } (1-\alpha_a)Re_p \geq 1000 \end{cases} \tag{3.35}$$

3.2 Kinetic Theory for granular flows

The Kinetic Theory for granular flows is a theory that extends the ideas and tools applied successfully for the kinetic theory of gases to flows characterized by dispersed particles. The dispersed particles are treated statistically, characterized by a frequency distribution of velocities and collisions, and the fluctuating velocities are then related to the shear gradient. The final outcome of the application of this model to the granular flow is a transport equation that describes the behaviour of a «granular temperature» Θ associated to the random movement of particles whose diffusion coefficients are given by (several different) empirical correlations.

The model implemented in Open source Field Operation And Manipulation (OpenFOAM) is derived from [41], a wide description of the theoretical background and applications of the KTGF is present in [43]. The notation in this section will follow the one proposed by [43].

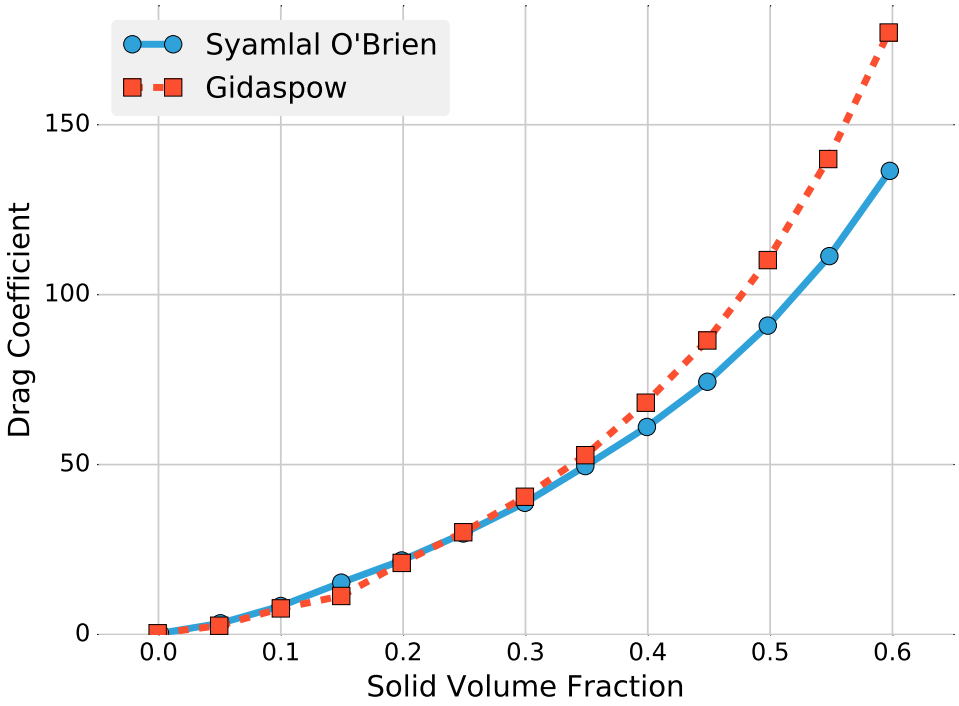

Figura 3.2: Comparison between drag models [41]

3.2.1 Governing Equations

The granular temperature is defined as a measure of the particle velocity fluctuations

$$\Theta = \frac{1}{3}\left\langle \mathbf{c}' \right\rangle \tag{3.36}$$

the $\langle\gamma\rangle$ operator is an averaging operator defined as

$$\langle\gamma\rangle = \frac{\int \gamma f \, \mathrm{d}\mathbf{c}}{n} \tag{3.37}$$

$$n = \int f \, \mathrm{d}\mathbf{c} \tag{3.38}$$

being f the frequency distribution of velocities, that is a function of time, position and instantaneous velocity

$$f = f\left(t, \mathbf{x}, \mathbf{c}\right) \tag{3.39}$$

The granular temperature behaviour is described by the Equation (3.40)

$$\begin{aligned} &\frac{3}{2}\left[\frac{\partial}{\partial t}\left(\alpha_s \rho_s \Theta_s\right) + \nabla \cdot \left(\alpha_s \rho_s \mathbf{u}_s \Theta_s\right)\right] = \\ &\underbrace{\left(-P_s \mathbf{I} + \boldsymbol{\tau}_s\right) : \nabla \mathbf{u}_s}_{\substack{\text{Production due to} \\ \text{shear stress}}} + \underbrace{\nabla \cdot \left(\kappa_\Theta \nabla \Theta\right)}_{\text{Diffusion}} \\ &- \underbrace{\gamma_\Theta}_{\substack{\text{Dissipation due to} \\ \text{inelastic collisions}}} + \underbrace{\Phi_\Theta}_{\substack{\text{Dissipation/Production} \\ \text{due to the interaction} \\ \text{with the carrier}}} \end{aligned} \tag{3.40}$$

where P_s is the granular pressure and represent the normal forces acting on the solid phase due to particle interactions. $\boldsymbol{\tau}_s$ is the stress tensor of the solid phase, κ_Θ is the granular conductivity, γ_Θ and Φ_Θ are two terms that describe production and/or dissipation of granular energy. Expression for all the terms can be derived [43]:

$$\boldsymbol{\tau}_s = \alpha_s \mu_s \left[\nabla \mathbf{u}_s + \nabla \mathbf{u}_s^T - \frac{2}{3}\left(\nabla \cdot \mathbf{u}_s\right)\mathbf{I}\right] + \left(-P_s + \lambda_s \nabla \cdot \mathbf{u}_s\right)\mathbf{I} \tag{3.41}$$

$$P_s = \rho_s \alpha_s \Theta \left[1 + 2\left(1+e\right) g_0 \alpha_s\right] \tag{3.42}$$

$$\lambda_s = \frac{4}{3}\alpha_s^2 \rho_s d_s g_0 \left(1+e\right)\sqrt{\frac{\Theta}{\pi}} \tag{3.43}$$

$$\gamma_\Theta = 12\left(1-e^2\right)\frac{\alpha_s^2 \rho_s g_0}{d_s\sqrt{\pi}}\Theta^{\frac{3}{2}} \tag{3.44}$$

$$\Phi_\Theta = \beta\left(3\Theta - \frac{\beta d_s \left|\mathbf{u}_r\right|^2}{4\alpha_s \rho_s \sqrt{\Theta\pi}}\right) \tag{3.45}$$

where λ_s is the bulk viscosity of the solid phase, e is the restitution coefficient that represents the percentage of momentum conserved after a collision between two particles, g_0 is a radial distribution function. β is the coupling coefficient for drag force that can be obtained from the interface drag exchange term:

$$\overline{\mathbf{M}}_a^{\text{drag}} = \alpha_a \frac{3}{4} \frac{\rho_b}{d_a} C_D \left|\mathbf{u}_r\right| \mathbf{u}_r = \beta \mathbf{u}_r \tag{3.46}$$

Expression for $\kappa_\Theta, \mu_s, g_0$ are given by several authors and summarized in Table 3.2.

3.2.2 Frictional Stress

When the solid phase fraction is high in a particular zone of the domain, lots of contacts among particles occurr and a frictional stress derives from them that must be accounted for in the mathematical model. In this state the collisions among particles could not be considered instantaneous as previously done in the kinetic theory and the frictional stress is accounted for adding a term in the granular pressure and in the granular viscosity:

$$P_s = P_{\text{kinetic}} + P_f \tag{3.47}$$

$$\mu_s = \mu_{\text{kinetic}} + \mu_f \tag{3.48}$$

A semi-empirical expression for the normal component of the frictional stress is given by [44]:

$$P_f = Fr \frac{(\alpha_s - \min(\alpha_s))^n}{\left(\alpha_{s,\max} - \alpha_s\right)^p} \tag{3.49}$$

where Fr, n, p are empirical constants. The frictional shear viscosity is than expressed by the Coulomb law:

$$\mu_f = P_f \sin\delta \tag{3.50}$$

being δ the *angle of internal friction of the particle*.

Another approach is suggested in [45] where the frictional normal stress is provided using the Equation (3.51) and the viscosity is then obtained by the Equation (3.52).

$$P_f = A(\alpha_s - \min(\alpha_s))^n \tag{3.51}$$

$$\mu_f = \frac{P_f \sin\delta}{\alpha_s \sqrt{\frac{1}{6}\left(\left(\frac{\partial u_s}{\partial x} - \frac{\partial v_s}{\partial y}\right)^2 + \left(\frac{\partial v_s}{\partial y}\right)^2 + \left(\frac{\partial u_s}{\partial x}\right)^2\right) + \frac{1}{4}\left(\frac{\partial u_s}{\partial y} + \frac{\partial v_s}{\partial x}\right)^2}} \tag{3.52}$$

Granular viscosity μ_s	
Syamlal et *al.*	$\frac{4}{5}\alpha_s^2\rho_s d_s g_0(1+e)\sqrt{\frac{\Theta}{\pi}} + \frac{1}{15}\sqrt{\Theta\pi}\rho_s d_s g_0 \frac{(1+e)\left(\frac{3}{2}e-\frac{1}{2}\right)}{\frac{3}{2}-\frac{e}{2}}\alpha_s^2 + \frac{1}{12}\frac{\alpha_s d_s \rho_s\sqrt{\pi\Theta}}{\frac{3}{2}-\frac{e}{2}}$
Gidaspow	$\frac{4}{5}\alpha_s^2\rho_s d_s g_0(1+e)\sqrt{\frac{\Theta}{\pi}} + \frac{1}{15}\sqrt{\Theta\pi}\rho_s d_s g_0(1+e)\alpha_s^2 + \frac{1}{6}\sqrt{\Theta\pi}\rho_s d_s \alpha_s + \frac{10}{96}\sqrt{\Theta\pi}\frac{\rho_s d_s}{(1+e)g_0}$
Lun et *al.*	$\frac{4}{5}\alpha_s^2\rho_s d_s g_0(1+e)\sqrt{\frac{\Theta}{\pi}} + \frac{1}{15}\sqrt{\Theta\pi}\frac{\rho_s d_s g_0(1+e)\left(\frac{3}{2}e-\frac{1}{2}\right)\alpha_s^2}{\frac{3}{2}-\frac{1}{2}e} + \frac{1}{6}\sqrt{\Theta\pi}\frac{\rho_s d_s \alpha_s\left(\frac{3}{4}e+\frac{1}{4}\right)}{\frac{3}{2}-\frac{e}{2}} + \frac{10}{96}\sqrt{\Theta\pi}\frac{\rho_s d_s}{(1+e)\left(\frac{3}{2}-\frac{1}{2}e\right)g_0}$
Granular conductivity κ_Θ	
Syamlal et *al.*	$2\alpha_s^2\rho_s d_s g_0(1+e)\sqrt{\frac{\Theta}{\pi}} + \frac{9}{8}\sqrt{\Theta\pi}\frac{\rho_s d_s g_0\left(\frac{1}{2}+\frac{e}{2}\right)^2(2e-1)\alpha_s^2}{\left(\frac{49}{16}-\frac{33}{16}e\right)} + \frac{15}{32}\sqrt{\Theta\pi}\frac{\alpha_s\rho_s d_s}{\left(\frac{49}{16}-\frac{33}{16}e\right)}$
Gidaspow	$2\alpha_s^2\rho_s d_s g_0(1+e)\sqrt{\frac{\Theta}{\pi}} + \frac{9}{8}\sqrt{\Theta\pi}\rho_s d_s g_0\left(\frac{1}{2}+\frac{e}{2}\right)\alpha_s^2 + \frac{15}{16}\sqrt{\Theta\pi}\alpha_s\rho_s d_s + \frac{25}{64}\sqrt{\Theta\pi}\frac{\rho_s d_s}{(1+e)g_0}$
Lun et *al.*	$2\alpha_s^2\rho_s d_s g_0(1+e)\sqrt{\frac{\Theta}{\pi}} + \frac{9}{8}\sqrt{\Theta\pi}\frac{\rho_s d_s g_0\left(\frac{1}{2}+\frac{e}{2}\right)^2(2e-1)\alpha_s^2}{\left(\frac{49}{16}-\frac{33}{16}e\right)} + \frac{15}{16}\sqrt{\Theta}\pi\frac{\alpha_s\rho_s d_s\left(\frac{e^2}{2}+\frac{1}{4}e+\frac{1}{4}\right)}{\left(\frac{49}{16}-\frac{33}{16}e\right)} + \frac{25}{64}\sqrt{\Theta\pi}\frac{\rho_s d_s}{(1+e)\left(\frac{49}{16}-\frac{33}{16}e\right)g_0}$
Radial Function g_0	
Lun and Savage	$\left(1-\frac{\alpha_s}{\alpha_{s,\max}}\right)^{-2.65\alpha_{s,\max}}$
Sinclair and Jackson	$\left[1-\left(\frac{\alpha_s}{\alpha_{s,\max}}\right)^{\frac{1}{3}}\right]^{-1}$
Gidaspow	$\frac{3}{5}\left[1-\left(\frac{\alpha_s}{\alpha_{s,\max}}\right)^{\frac{1}{3}}\right]^{-1}$

Tabella 3.2: Kinetic Theory Correlations

3.2.3 Johnson and Jackson BCs

The solid phase does not behave as the classical liquid on the walls, that means the classical *no-slip* condition that it is usually used on the walls for a liquid is not considered correct for a particulate. Instead, in [44] is proposed a different boundary condition on walls that allows non-zero velocities on the boundary. The derivation is done considering the balance of the tangential force per unit area exerted on the boundary by the particles and the corresponding stress within the particle assembly near the boundary. The tangential force is assumed to be (Coulomb's law of friction applied to the material sliding on the surface):

$$T_f = N_f \tan\delta \tag{3.53}$$

where N_f is the normal component of the frictional stress. The rate of transfer of momentum to unit area of the surface due to collisions is given by the collisional frequency of particles $\sqrt{3\Theta}/s$ times the average tangential momentum exchanged per collision $\left(\phi\rho_p V_p \mathbf{u}_{\text{slip}}\right)$ and the number of particles adjacent to the unit area of the surface $1/a_c$. s is the average distance of a particle surface from the wall boundary, $\mathbf{u}_{\text{slip}}$ is the difference between the velocity of the particle and the velocity of the wall $(\mathbf{u}_s - \mathbf{u}_{\text{wall}})$, a_c is the average boundary area per particle, ρ_p and V_p are respectively the density and the volume of the particle $\left(\text{that is assumed to be spherical } V_p = 1/6\pi d_p^3\right)$, ϕ is a *specularity coefficient* that is dependant from the average roughness of the surface and its values range from 0 (perfect specular collision) to 1 (perfect diffuse collisions). In other words ϕ is a measure of the amount in percentage of tangential momentum lost in a collision with the wall. Both s and a_c are functions of the solid phase fraction:

$$s = d_p\left[\left(\frac{\alpha_{s,\max}}{\alpha_s}\right)^{\frac{1}{3}} - 1\right] \tag{3.54}$$

$$a_c = d_p^2\left(\frac{\alpha_{s,\max}}{\alpha_s}\right)^{\frac{2}{3}} \tag{3.55}$$

In this case the expression $\alpha_{s,\max}$ stands for the *phase fraction at maximum packing condition* that is generally taken to be 0.65.

Equating all the contributions projected along the $\frac{\mathbf{u}_{\text{slip}}}{|\mathbf{u}_{\text{slip}}|}$ direction gives the first boundary condition for the particles velocity at wall.

$$\frac{\mathbf{u}_{\text{slip}} \cdot \left(\boldsymbol{\sigma}_{\text{kinetic}} + \boldsymbol{\sigma}_f\right) \cdot \hat{\mathbf{n}}}{\left|\mathbf{u}_{\text{slip}}\right|} + \frac{\sqrt{3}\phi\rho_p\pi\sqrt{\Theta}\left|\mathbf{u}_{\text{slip}}\right|}{6\alpha_{s,\max}\left[1 - \left(\frac{\alpha_s}{\alpha_{s,\max}}\right)^{\frac{2}{3}}\right]} + N_f \tan\delta = 0 \tag{3.56}$$

In Equation (3.56) the first element in the Left Hand Side (LHS) is the total stress component along the $\mathbf{u}_{\text{slip}}$ direction, the second is the collisional contribution to momentum balance, the third is the frictional force in the same direction. $\boldsymbol{\sigma}_{\text{kinetic}} + \boldsymbol{\sigma}_f$ is the total stress tensor defined in the compressive sense, made by a collitional and a frictional contribution as reported in the introduction of [44].

Making a similar balance over the control volume showed in Figure 3.3 for the total energy and the «true» energy (opposed to the «pseudo-thermal» energy associated to the fluctuations of particles – analogy to the kinetic theory of gases) Equation (3.57) and Equation (3.58) are obtained.

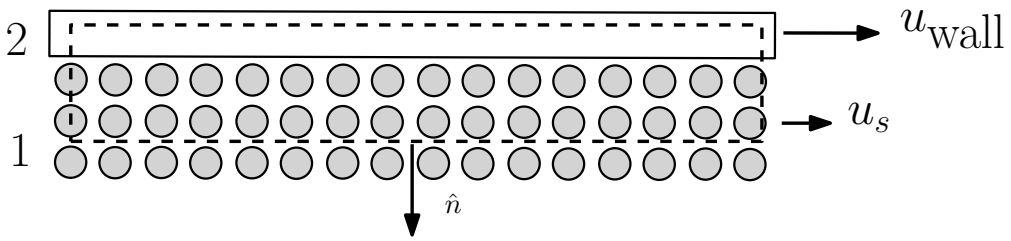

Figura 3.3: Control volume for the the energy flux BC [44]

$$-\hat{\mathbf{n}}\cdot\hat{\mathbf{q}}|_1-\mathbf{u}_s\cdot(\boldsymbol{\sigma}\cdot\hat{\mathbf{n}})|_1+\hat{\mathbf{n}}\cdot\hat{\mathbf{q}}|_2+\mathbf{u}_{\text{wall}}\cdot(\boldsymbol{\sigma}\cdot\hat{\mathbf{n}})|_2=0 \tag{3.57}$$

$$-\hat{\mathbf{n}}\cdot\mathbf{q}|_1+\hat{\mathbf{n}}\cdot\mathbf{q}|_2+\mathscr{D}-\mathbf{u}_{\text{slip}}\cdot\mathbf{S}_f^b=0 \tag{3.58}$$

$\hat{\mathbf{q}}=\mathbf{q}+\mathbf{q}_{\text{PT}}$ is the total heat flux composed by the summation of a true thermal heat flux $\mathbf{q}$ and a pseudo-thermal one $\mathbf{q}_{\text{PT}}$.
$\mathscr{D}$ is the rate of dissipation of pseudo-thermal energy due to inelastic collisions of particles with the unit area of the boundary whose expression is given in Equation (3.60). The last term is the frictional heating caused by particles sliding over the surface. $\mathbf{S}^b=\boldsymbol{\sigma}\cdot\hat{\mathbf{n}}=\mathbf{S}_c^b+\mathbf{S}_f^b$ is the total force per unit area arising from kinetic and frictional contribution. Subtracting the two equations, Equation (3.59) is obtained.

$$-\hat{\mathbf{n}}\cdot\mathbf{q}_{\text{PT}}=\mathscr{D}+\mathbf{u}_{\text{slip}}\cdot\mathbf{S}_c^b \tag{3.59}$$

$\mathbf{S}_c^b$ is the force per unit area acting on the boundary due to collisions, and it is already derived in the second term of the Equation (3.56). The only expression that is missing is for $\mathscr{D}$, that is given by the energy loss per particle collision with the wall $(1-e_w)\rho_p V_p\frac{3}{2}\Theta$, the collision frequency and the number of particles adjacent to the unit area of the wall surface as already given before.

$$\mathscr{D}=\left[\frac{1}{4}\pi\rho_p d_p^3\Theta(1-e_w)\right]\left[\frac{\sqrt{3\Theta}}{d_p\left[\left(\frac{\alpha_{s,\max}}{\alpha_s}\right)^{\frac{1}{3}}-1\right]}\right]\left[\frac{1}{d_p^2\left(\frac{\alpha_{s,\max}}{\alpha_s}\right)^{\frac{2}{3}}}\right] \tag{3.60}$$

e_w is the *restitution coefficient* of the wall, i.e. the amount of normal momentum lost hitting the wall.

In this section Equation (3.56) and Equation (3.59) have been described, those are the boundary conditions to be applied respectively to the $\mathbf{u}_s$ and Θ fields in the comprehensive system of resolving equations of the problem under examination.

3.3 Validation

A numerical model, to be useful for industrial application, must be validated on experimental data and/or on other validated numerical results (e.g. Direct Navier-Stokes Simulation (DNS)). Experimental data for slush flows are not so common in literature and in addition, apart from the data

available about the pressure drops in pipe geometries, the sampling of the phase fractions and the solid phase velocity is somehow problematic due to the intrinsic choking tendency of probes for this king of flows and to the low temperatures needed for the production and use of those kind of flows. However in the documents collected by the author, the most promising techniques to sample consistently those properties is the Particle Image Velocimetry (PIV). In [25] the validation is carried on using PIV together with experimental outcomes from [12], [26], meanwhile in [44] only the mean values are sampled. No profiles are given. The work in [1] is also showing mean parameters, no profiles.

Capitolo 4

Correlations and Engineering Models

Flows with dispersed particulate within a liquid carrier are of big importance in the industrial framework. For this reason, next to more computational intensive toolset fast and reliable engineering models are also needed to perform preliminary size and estimations.

For what concerns slush flows, empirical correlations and tools are very rare, the only example that was possible to find is a tool developed by NASA named FLow of slUSH (FLUSH) for sizing of pipelines of SLH2 in the frame of Shuttle program and later ones (e.g. NASP) briefly mentioned in Section 4.1.

Widening the point of view to general slurry flows, the situations improves and several correlations and models are available in the literature, both purely empirical and mechanistic semi-empirical attempts that show conflicting applicability in dependency to the various problem properties (e.g. solid-liquid density ratio, pipe diameter, ...).
Nonetheless, assuming that a slush flow could be modeled as a slurry flow – and this might be considered as an hazardous assumption since the shape of solid particles is not well determined in slush flows and it is still debatable that the behavior of a slush flow could be compared in analogy to slurry flows – when interested to the hydrodynamic behavior, that means neglecting the very important feature of phase change, could be a first step towards the set up of a correlation or engineering model for slushes. A good overview on empirical correlations is reported in [46].

In this section a brief evaluation of some experimental correlation available to estimate pressure drops and nature of the flow for slurries is performed and discussed. A lightweight Python library named `pyslurry` is also introduced.

4.1 FLow of slUSH

At NASA a software tool named FLUSH was developed to calculate pressure drops and solid fraction losses within different elements of a pipeline system of SLH2 solving one-dimensional steady-state energy equation Equation (4.1) and Bernoulli's equation Equation (4.2) [47].

$$\Delta\left(h+\frac{|\mathbf{u}|^2}{2}+gz\right)=\frac{\dot{Q}}{\dot{m}}-W_s \tag{4.1}$$

$$\Delta\left(\frac{p}{\rho}+\frac{|\mathbf{u}|^2}{2}+gz\right)+W_s=0 \tag{4.2}$$

where W_s is the shaft work $\left[\frac{\mathrm{J}}{\mathrm{kg}}=\frac{\mathrm{m}^2}{\mathrm{s}^2}\right]$

The thermo-physical properties of the SLH2 are retrieved using `GASPLUS`, a `FORTRAN 77` program described in [48]. The software allows the user to specify several different elements of the pipeline like elbows, valves and straight pipe segments, and is equipped with the capability of heat-leaks automated calculation for vacuum-jacketed piping if not available.

The assumption made in the model which the program is based on are reported to be:

- Steady-state flow exists in the system
- Fluid is incompressible
- Lines are pre-cooled to TP
- Slush is well-mixed at the entrance of the line and settling effects are neglected
- The viscosity of the slush is equal to the LH2 (since the SLH2 viscosity is unknown)
- Heat of fusion is a constant
- Heat flux is used first (and only) to melt solids in a isotherm and constant pressure process

The algorithm pseudo-code described in [47] is reported in Algorithm 1.

4.2 Durand and Condolios

Durand and Condolios are one of the pioneers in the field of slurry flows. They carried out several experiments on sands and gravels whose results are explained in [49]. The original correlation is written in terms of relative head loss (Equation (4.3)), being i_{slurry} the head loss of the slurry, i_{pure} the head loss of the relative pure fluid (e.g. water), C the volumetric concentration of the solids.

$$\frac{i_{\text{slurry}}-i_{\text{pure}}}{i_{\text{pure}}C}=\frac{\Delta p_{\text{slurry}}-\Delta p_{\text{pure}}}{\Delta p_{\text{pure}}C}=\Phi \tag{4.3}$$

In [46] a modification of the original correlation is reported, suggested by Gibert, to be as in Equation (4.4).

$$\Phi=K\psi^{-\frac{3}{2}} \tag{4.4}$$

Algorithm 1 FLUSH algorithm for computation of SLH2 [47]

Initialize temperatures, pressures, slush solid fraction, heat leak, element length, diameter and height
while $Y_i > 0$ and $\text{err}(p, T) < \text{tol}$ **do**
    Use `GASPLUS` to obtain initial-element SLH2 properties
    $\rho_l = \rho_l(T_i, p_i)$
    $\mu_l = \mu_l(T_i, p_i)$
    Calculate an effective slush density at the inlet
    $\rho_{\text{mix}} = Y_i \rho_s + (1 - Y_i)\rho_l$
    Calculate mass flow rate and Reynolds number (using liquid viscosities)
    Calculate a friction factor using the Darcy-Weisbach correlation or National Institute of Standards and Technology (NIST)'s slush correlations
    Calculate the downstream pressure from Bernoulli's equation
    $p_f = p_i + \Delta p$
    Obtain final-element hydrogen properties from `GASPLUS`
    $\rho_l = \rho_l(T_f, p_f)$
    $\mu_l = \mu_l(T_f, p_f)$
    Obtain initial and final enthalpies from `GASPLUS`
    $H_{l,f} = H_{l,f}(T_f, p_f)$
    $H_{l,i} = H_{l,i}(T_i, p_i)$
    Calculate initial mixture enthalpy
    $H_{\text{mix},i} = H_{l,i} - Y_i H_{\text{fus}}$
    Calculate final mixture enthalpy from energy equation
    $H_{\text{mix},f} = H_{\text{mix, i}} + \Delta H$
    Calculate the change in slush solid fraction due to heat
    $Y_{f,\text{heat}} = \frac{H_{l,f} - H_{\text{mix},f}}{H_{\text{fus}}}$
    Calculate the change in slush solid fraction due to friction
    $\Delta Y_{\text{frict}} = \frac{f}{H_{\text{fus}}^J}$
    Calculate the slush fraction at the element exit
    $Y_f = Y_{f,\text{heat}} - \Delta Y_{\text{frict}}$
end while

$$\psi = Fr_{\text{fl}}^2 \, Fr_p^{-1} \tag{4.5}$$

$$Fr_p = \frac{1}{\sqrt{C_x}} = \frac{v_t}{\sqrt{g d_p}} \tag{4.6}$$

$$Fr_{\text{fl}} = \frac{u}{\sqrt{gD\eta}} \tag{4.7}$$

$$\eta = \frac{\rho_p}{\rho_l} \tag{4.8}$$

where g is the gravitational field, v_t is the *terminal settling velocity of the particles*, d_p the diameter of the particles, D the hydraulic diameter of the duct, ρ_p and ρ_l the densities of the particle and the carrier liquid respectively, u the velocity of the slurry. The modification suggested by Gibert lies in the definition of the flow Froude number F_{fl} since in the original paper by Durand and Condolios [49] that number is defined without the density ratio η at the denominator.

4.2.1 Terminal Velocity correlations

The Durand and Condolios correlation reported in Equation (4.4) needs an estimation of the terminal velocity of the particles v_t, or equivalently, of the drag coefficient C_D, since by the definition of the terminal velocity (informally «the terminal velocity is the velocity for which the gravitational force equates the buoyancy and drag forces») the two parameters are related by Equation (4.9).

$$C_D = \frac{4}{3} \frac{(\eta - 1)\, g}{v_t^2} \tag{4.9}$$

In the original paper few hints are given, often in terms of graphs relating the Froude numbers, while in [46] the Zanke correlation for the terminal velocity is used (Equation (4.10)). Several correlations are analyzed in [50] and another correlation, this time for the drag coefficient, is given by [51] and reported in Equation (4.11) and Equation (4.12) for convenience.

$$v_t = \frac{10\, \nu_l}{d_p} \left[\left(1 + 0.01 \frac{(s-1)\, g d^3}{\nu_l^2} \right)^{0.5} - 1 \right] \tag{4.10}$$

$$\Lambda = Re_p \sqrt{C_D} = \left[\frac{4}{3} \frac{g d_p^3 \rho_l (\rho_s - \rho_l)}{\mu_l} \right] \tag{4.11}$$

$$\log_{10}\left(Re_p\right) = -1.38 + 1.94 \log_{10} \Lambda - 8.60\text{e}{-2} \log^2 \Lambda - 2.52\text{e}{-2} \log^3 \Lambda + 9.19\text{e}{-4} \log^4 \Lambda + 5.35\text{e}{-4} \log^5 \Lambda \tag{4.12}$$

The prediction quality of the Durand-Condolios correlation together with the two Zanke and Turian drag estimation are showed in Figure 4.1.
The quality of prediction is not satisfying also considering that the cross-check data are collected by the original work of Durand. The computation is performed using `pyslurry` library, a brief user guide is referred in Chapter A.

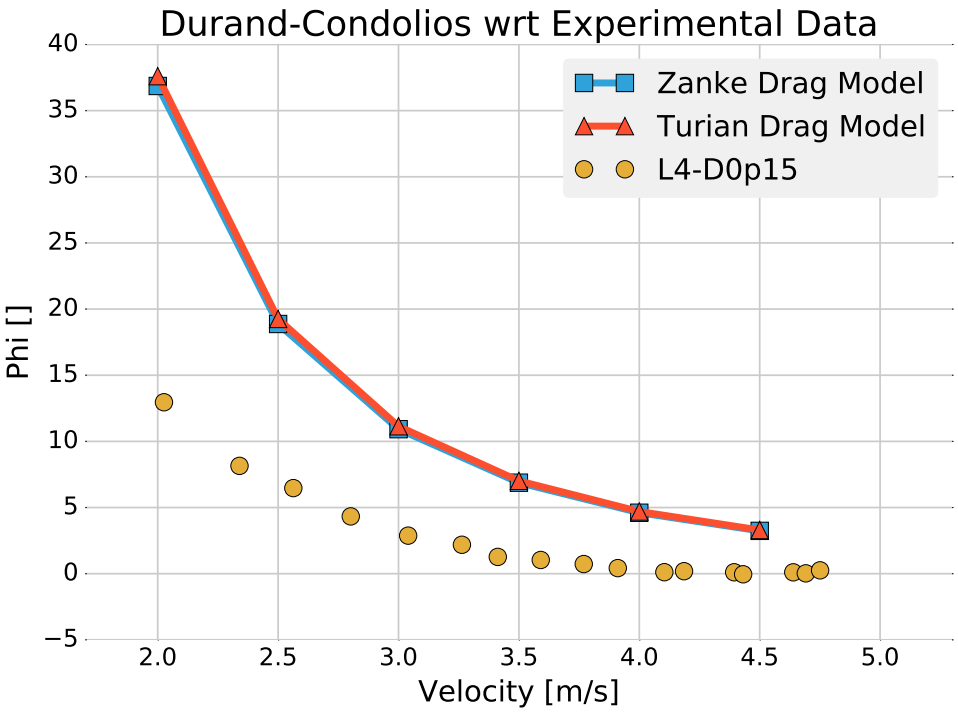

(a) Durand-Condolios Estimation for L4 Sands

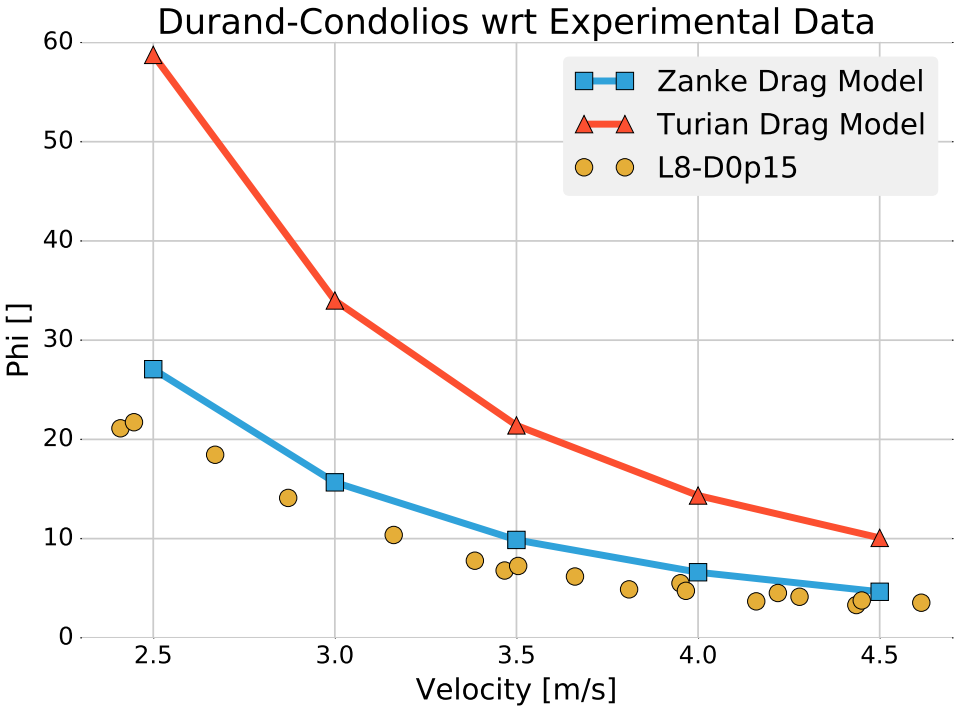

(b) Durand-Condolios Estimation for L8 Sands

Figura 4.1: Durand-Condolios correlation prediction on L4, L8 Sands

4.3 Turian and Yuan Correlations

Another example of correlations for slurry flows is given by Turian *et al.* in [51]. Differently from what Durand *et al.* did, Turian and coworkers provide different correlations for different regime of slurry flow, together with means to estimate the nature of flow on the basis of typical parameters characterizing a slurry. In that work, four different regimes are identified: *flow with a stationary bed*, *saltation flow*, *heterogeneous flow*, *homogeneous flow*, those regimes can be delineated computing some regime numbers R_{ij}, when these regime numbers reach the value of 1, transition occurs. The functional structure of this regime numbers is given by Equation (4.13).

$$R_{ij} = \frac{u^2}{k_1 C^{n_1} f_w^{n_2} C_D^{n_3} Dg(\eta - 1)} \tag{4.13}$$

where k_1, n_1, n_2, n_3 are empirical parameters given by the paper. f_w is the Fanning friction factor of the associated pure liquid. An example for the regime number associated to the transition from *stationary bed* (0) to *saltation* (1) is given in Equation (4.14).

$$R_{01} = \frac{u^2}{31.93 C^{1.083} f_w^{1.064} C_D^{-0.06160} Dg(\eta - 1)} \tag{4.14}$$

Once the regime is identified, specific pressure-drop correlations can be applied. The pressure drop is given relatively to the friction factor of the associated pure fluid of the slurry (i.e. water) and the functional form of a pressure drop correlation is of the type:

$$f - f_w = \hat{k}_1 C^{\hat{n}_1} f_w^{\hat{n}_2} C_D^{\hat{n}_3} \left[\frac{u^2}{Dg\,(\eta - 1)} \right]^{\hat{n}_4} \tag{4.15}$$

Also considering the higher flexibility of the correlations provided by Turian and coworkers, from tests performed on several different dataset of slurries, the results are not satisfying. The regime delineation often failed in the correct determination of the flow, hence predicting wrong pressure drops. In addition to that, in a future work always by Turian *et al.* [52], the same correlations are cross-referenced, but they appear with a different prefactor, for example for stationary bed regime:

$$f - f_w = 0.4936 C^{0.7389} f_w^{0.7717} C_D^{-0.4054} \left[\frac{u^2}{Dg\,(\eta - 1)} \right]^{-1.096} \quad [51] \tag{4.16}$$

$$f - f_w = 12.127 C^{0.7389} f_w^{0.7717} C_D^{-0.4054} \left[\frac{u^2}{Dg\,(\eta - 1)} \right]^{-1.096} \quad [52] \tag{4.17}$$

$$\tag{4.18}$$

That circumstance raises some doubts about the correctness of the formulas, also considering that the difference between the two prefactors are not constant among the different correlations leading to some sort of ambiguity. Still, the model of Turian has been coded in `pyslurry` with the hope that community contributions could help to clarify the situation.

Capitolo 5

Results

Several different runs of simulations have been performed as benchmark of the model. Since not many experimental data for slush flows are available in literature, together with configuration with SLN2, also cases run for a «more classical» water-glass-beads have been performed comparing the results with the experimental data available on [53].

A sensitivity analysis on the Kaushal case has been performed to compare the effect of the various parameters that can be tuned in the KTGF in addition to the effects of mesh and turbulence models.

5.1 Notes on Convergence

`twoPhaseEulerFoam` is a transient solver, it is not possible to set up a steady state as differently it is possible on FLUENT. To keep the two kind of simulations as similar as possible, the convergence criterion has been established to stop the simulation when the pressure drop across the pipe reach a steady value. An example of a pressure drop profile over simulated time with a zoom over the last time iterations is reported in Figure 5.1. As it is possible to see, the pressure drop keeps oscillating as if it was the response of an undamped marginally stable harmonic system, for this reason the final value of the pressure drop reported in the next sections has been calculated as a mean value of the last 400 time iterations.

For what concerns the numerical schemes, the `twoPhaseEulerFoam` solver in OpenFOAM is very irritable, the mesh has to be very smooth and for the simulations performed in this work, the Aspect Ratio (AR) has not to exceed a value of ~ 20 or the pressure calculations started to oscillate leading very often to divergence and crash. In order to account for this intrinsic sensitivity to the mesh, first-order schemes (upwind) have been chosen for all the fluxes (`divSchemes` in OpenFOAM) to obtain as stability as possible. Another important parameter to monitor is the Courant Number Co, value too near to 1 led to instability and divergence in particular at the starting up. This is probably also addressable to the semi-implicit nature of the MUlti-dimensionsal Limiter for Explicit Solution (MULES) solver for the phase fraction equation used in OpenFOAM. As a probably too conservative rule in the following simulations the Co has been constrained to not be greater than 0.5.

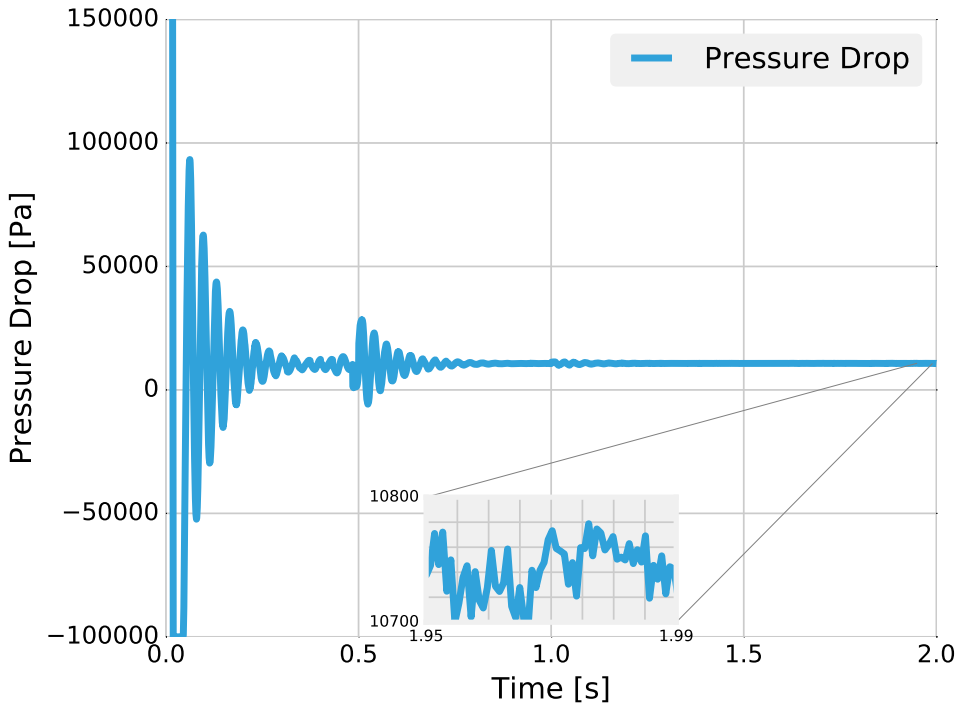

Figura 5.1: Pressure drop profile over time

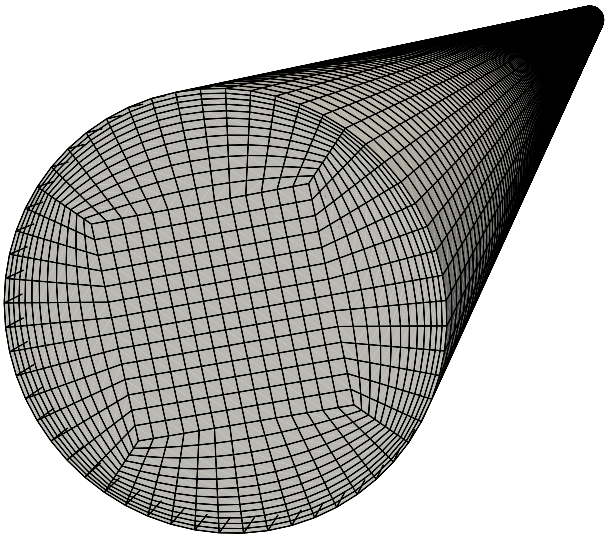

Figura 5.2: Base mesh for all the cases

5.2 Initial and Boundary Conditions

The mesh for all the simulations, both for the Kaushal and slush case, is created using the `blockMesh` utility provided by OpenFOAM using a parametrizable `cylinder.m4` or `halfcylinder.m4` file that is compiled using the GNU m4 macro preprocessor, allowing to change the geometrical dimensions of the mesh and the number of cells per block easily. `blockMesh` creates structured mesh made of hexahedral blocks. An example of the mesh is shown in Figure 5.2.

The mesh is composed respectively by 3 different patches (`inlet`, `outlet` and `walls` for the normal full-size cylinder, by 4 instead for the half-cylinder (the fourth patch is the symmetry plane). BCs for all the fields must be set on all the patches and for the initial internal field. For the `inlet` patch, uniform constant profiles have been configured for all the fields. Also constant profiles are provided for initialization of the internal field. On the walls, for the turbulent fields $k, \epsilon, \omega, \nu_t$ wall functions are used since $y^+ > 30$ averagely over all the domain. At the `outlet` the gradients of all the fields are fixed to zero (except for the pressure that has instead a fixed value since it is not possible to fix both the pressure and the velocity on the same boundary - it would cause an over-constrained problem). The BCs are summarized in Table 5.1.

Field	inlet	outlet	walls	symmetryPlane	internalField
α_s	fixed value	zero gradient	zero gradient	symmetry	fixed value
ϵ_l	mixing length law	zero gradient	wall function	symmetry	fixed value
k_l	turbulence intensity	zero gradient	wall function	symmetry	fixed value
$\nu_{t_s}^{\text{OF}}$	calculated	calculated	calculated	symmetry	fixed value
$\nu_{t_l}^{\text{OF}}$	calculated	calculated	wall function	symmetry	fixed value
ω_l	fixed value	zero gradient	wall function	symmetry	fixed value
p	zero gradient	fixed value	zero gradient	symmetry	fixed value
Θ_p	fixed value	zero gradient	Johnson - Jackson BC	symmetry	fixed value
$\mathbf{u}_s$	$\begin{pmatrix} 0 & u_{s_y} & 0 \end{pmatrix}$	zero gradient	Johnson - Jackson BC	symmetry	fixed value
$\mathbf{u}_l$	$\begin{pmatrix} 0 & u_{l_y} & 0 \end{pmatrix}$	zero gradient	no slip	symmetry	fixed value

[OF] Specific to OpenFOAM since FLUENT takes care of it by itself.

Tabella 5.1: Boundary Conditions Summary

5.3 Pure Water

As first validation of the `twoPhaseEulerFoam` solver, a case with pure water, without any solid phase inside, has been run. The test domain was a 3 m long, 55 mm of diameter pipe. The mesh was built of a cross-section made by an internal square of 16×16 cells, 4× circular sectors of 16×14 cells, and 500 cells lengthwise for a total count of 576000 cells. The inlet velocity is 3.0 m/s, the turbulence model is the $k-\epsilon$ with standard wall functions as wall treatment.

The velocity profile is shown in Figure 5.3 and the relative pressure drop comparison is reported in Table 5.2 together with the estimated value by the Darcy-Weisbach equation (Equation (5.1)) and the Colebrook equation (Equation (5.2)) for the estimation of the friction factor (that is a trascendent equation that is solved using the `MINPACK`'s `HYBRD-HYBRDJ` zeroes-finding algorithm wrapped by Python's `scipy.optimize.fsolve` method).

$$\frac{\Delta P}{L} = \frac{1}{2}\frac{f}{D}\rho_l u_l^2 \tag{5.1}$$

$$\frac{1}{\sqrt{f}} + 2.0\log_{10}\left(\frac{\xi/D}{3.7} + \frac{2.51}{Re\sqrt{f}}\right) = 0 \tag{5.2}$$

The theoretical velocity profile is well-reproduced and the pressure-drop records a $\sim 2.5\%$ error with respect to the value estimated by the Darcy-Weisbach equation. The mesh setup and the boundary conditions for the liquid phase are in this way demonstrated to be coherent with the physics of the problem. The same behavior is found also for different inlet velocities (always in the turbulent regime) confirming the correct setup of the solver for the liquid phase.

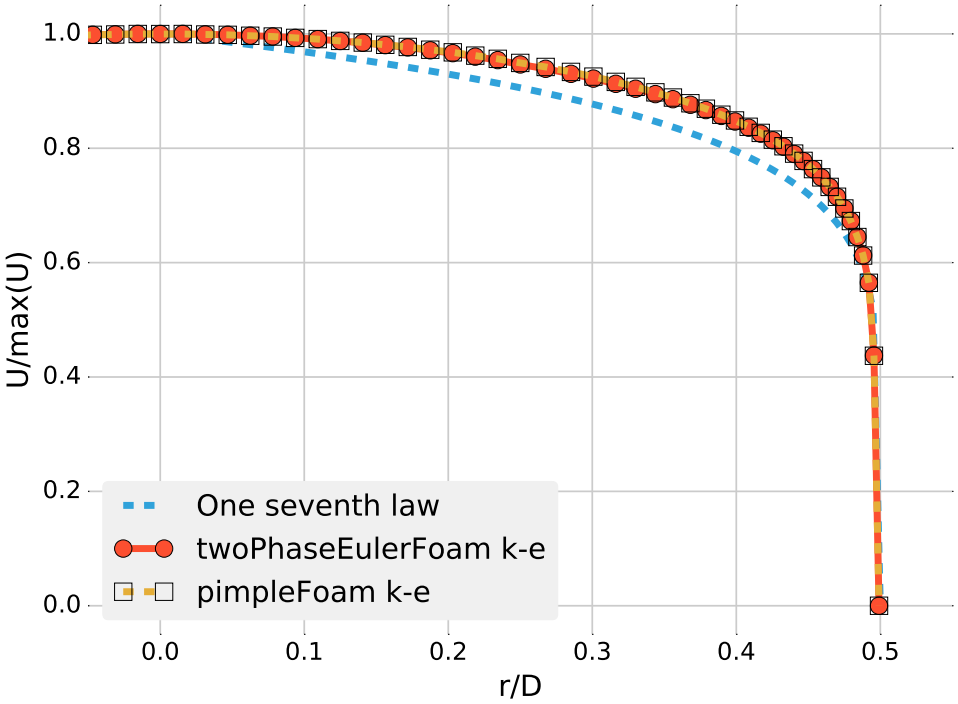

Figura 5.3: Velocity profile for pure water

`twoPhaseEulerFoam`	`pimpleFoam`	Darcy-Weisbach
1361.2	1382.9	1330.5

Tabella 5.2: Pure water pressure drop

Pipe Diameter [mm]	**Liquid Viscosity** [Pa s]	**Solid Density** $\left[\frac{kg}{m^3}\right]$	**Liquid Density** $\left[\frac{kg}{m^3}\right]$
55	1e−3	2470	1000

Tabella 5.3: Kaushal case properties

5.4 Water-Glass-Beads slurry (Kaushal)

The first multiphase case simulated using OpenFOAM is a more classical, with respect to slush flows, slurry flow characterized by water as liquid carrier and glass-beads as solid particulate.
The choice to perform an analysis of this kind has been driven by the fact that the shape of the particles in this case is well-established to be spherical and also because more experimental data are available in literature. In Table 5.3 the geometric and thermo-physical properties of the case are reported.

The benchmark case chosen is the one reported in [53]. First of all a sensitivity analysis over the several parameters that could be tuned in the KTGF is performed, the most important effects of parameters variation are highlighted. Then a complete set of simulations is performed and is compared with experimental data from [53].

5.4.1 Sensitivity analysis for the KTGF

In the Section 3.2 the Kinetic Theory for granular flows is presented. From the details there described is clear as there are several parameters that can be modified and that can influence the results of the simulation. In the literature analyzed some suggestions are given about few parameters, in particular the restitution coefficient e and the specularity coefficient ϕ, both for walls bouncing and internal collisions, in [29] are taken with the values of, respectively, of $e_w = 0.99$, $e = 0.9$, $\phi = 0.0001$ while in [21] $\phi = 0.02$. Moreover a maximum packing limit for the phase fraction is given $\alpha_{max} = 0.52$ for slush nitrogen. It's clear as those parameters show a behaviour that is strongly case-specific, hence the need for a sensitivity analysis over the several different tunable parameters and models has emerged. A summary of the different modifications done is summarized in Table 5.4 in terms of effects on the pressure drop along the pipe.

From the analysis of Table 5.4 is possible to understand how the most important parameter, in terms of influence over the pressure drop, is the specularity coefficient ϕ. This importance could be easily understood since ϕ represents the amount in percentage of tangential momentum loss at the wall. As in a «normal» pure-liquid situation where the viscosity and the boundary layer that it is created near the wall influence the pressure loss, also here the wall interaction is very important even if the physical process that creates the momentum loss is not fully related to friction, but also to collisions of solid particles with the wall itself (see Section 3.2.3).

Pressure drop is not the only property of interest. Also the distribution of the solid phase along the diameter in a cross-section and the velocity profile are interesting. A selection of cases are compared in terms of velocity profiles in Figure 5.4 and in terms of phase fraction dispersion over the diameter in Figure 5.5. Moreover a comparison between the Gidaspow and the Syamlal model is also shown in Figure 5.6 and Figure 5.7.

Case Name	Particle Diameter [mm]	Drag Model	Viscosity	Conductivity	Granular Pressure	Frictional Model	Radial Model	δ	$\alpha_{\max}$	e	e_w	ϕ	Y^+	$\frac{\Delta P}{L}\left[\frac{\text{Pa}}{\text{m}}\right]$
gidasphi	44e−3	Gidaspow-Ergun-WenYu	Gidaspow	Gidaspow	Lun	Schaeffer	SinclairJackson	30	0.64	0.9	0.9	0.01	37	2309
gidasphi075	44e−3	Gidaspow-Ergun-WenYu	Gidaspow	Gidaspow	Lun	Schaeffer	SinclairJackson	30	0.64	0.75	0.9	0.01	37	2249
gidasphie	44e−3	Gidaspow-Ergun-WenYu	Gidaspow	Gidaspow	Lun	Schaeffer	SinclairJackson	30	0.64	0.9	0.2	0.01	37	2309
gidasphie099	44e−3	Gidaspow-Ergun-WenYu	Gidaspow	Gidaspow	Lun	Schaeffer	SinclairJackson	30	0.64	0.9	0.99	0.01	37	2309
gidasphiam	44e−3	Gidaspow-Ergun-WenYu	Gidaspow	Gidaspow	Lun	Schaeffer	SinclairJackson	30	0.5	0.9	0.9	0.01	37	4329
gidasphiam0001	44e−3	Gidaspow-Ergun-WenYu	Gidaspow	Gidaspow	Lun	Schaeffer	SinclairJackson	30	0.5	0.9	0.9	0.001	37	1965
gidasphi002	44e−3	Gidaspow-Ergun-WenYu	Gidaspow	Gidaspow	Lun	Schaeffer	SinclairJackson	30	0.64	0.9	0.9	0.02	43	3354
gidasphi005	44e−3	Gidaspow-Ergun-WenYu	Gidaspow	Gidaspow	Lun	Schaeffer	SinclairJackson	30	0.64	0.9	0.9	0.05	43	7137
gidasnofrict	44e−3	Gidaspow-Ergun-WenYu	Gidaspow	Gidaspow	Lun	Schaeffer	SinclairJackson	0	0.64	0.9	0.9	0.01	36	2239
gidasfr25	44e−3	Gidaspow-Ergun-WenYu	Gidaspow	Gidaspow	Lun	Schaeffer	SinclairJackson	25	0.64	0.9	0.9	0.01	37	2255
gidasphijj	44e−3	Gidaspow-Ergun-WenYu	Gidaspow	Gidaspow	Lun	JohnsonJackson	SinclairJackson	28.5	0.64	0.9	0.9	0.01	37	2290
gidasphijj002	44e−3	Gidaspow-Ergun-WenYu	Gidaspow	Gidaspow	Lun	JohnsonJackson	SinclairJackson	28.5	0.64	0.9	0.9	0.02	37	3122
gidasphils	44e−3	Gidaspow-Ergun-WenYu	Gidaspow	Gidaspow	Lun	Schaeffer	LunSavage	30	0.64	0.9	0.9	0.01	37	2229
gidasphismall	1.25e−4	Gidaspow-Ergun-WenYu	Gidaspow	Gidaspow	Lun	Schaeffer	SinclairJackson	30	0.64	0.9	0.9	0.01	43	3650
gidasphigibilaro	44e−3	Gibilaro	Gidaspow	Gidaspow	Lun	Schaeffer	SinclairJackson	30	0.64	0.9	0.9	0.01	37	2478
syamlal	1.25e−4	Syamlal-OBrien	Syamlal	Syamlal	Syamlal-Rogers-OBrien	Schaeffer	SinclairJackson	30	0.64	0.9	0.9	0.01	43	3580
syamlaljj	1.25e−4	Syamlal-OBrien	Syamlal	Syamlal	Syamlal-Rogers-OBrien	JohnsonJackson	SinclairJackson	28.5	0.64	0.9	0.9	0.01	43	3580
syamlaljj002	1.25e−4	Syamlal-OBrien	Syamlal	Syamlal	Syamlal-Rogers-OBrien	JohnsonJackson	SinclairJackson	28.5	0.64	0.9	0.9	0.02	43	3880
syamlaljj0001	1.25e−4	Syamlal-OBrien	Syamlal	Syamlal	Syamlal-Rogers-OBrien	JohnsonJackson	SinclairJackson	28.5	0.64	0.9	0.9	0.001	43	3431

$u = 3.0\frac{\text{m}}{\text{s}}, \alpha = 0.30, \alpha_{\min_f} = 0.5$, Turbulence model: $k-\epsilon$.
In black the modifications with respect to the base case that is `gidasphi`.

Tabella 5.4: Sensitivity Analysis for Kaushal Case

Model	Particle Diameter [mm]	δ	α_{max}	e	e_w	ϕ
Gidaspow Model	44e−3	28.5	0.5	0.9	0.9	0.001
Syamlal Model	44e−3	28.5	0.5	0.9	0.9	0.01

Tabella 5.5: Settings for Kaushal case

From the sensitivity analysis it is possible to understand how the maximum packing limit α_{max} and the radial model have a strong impact on the velocity profile in particular. The profile for the lower α_{max} (`gidasphiam`) tends more to the typical profile of a pure liquid but the pressure drop is doubled with respect to the base case, leading to unrealistic values. This behavior can be hindered tweaking with the value of the specularity coefficient (`gidasphiam0001`), but the effect on the velocity profile is also reduced. Focusing the attention to the phase fraction profiles instead, the effects of the different packing limit are somehow lower, the shape of the α fraction is kept changing all the parameters, with minor differences in the slope: the case that implements a different radial distribution function model (`gidasjj`) shows a smoother slope passing from the zone of the pipe (on the bottom) with higher density of particles to the upper part that does not contain solids.

The comparison between the Gidaspow model and the Syamlal model (Figure 5.6, Figure 5.7) is performed with a different, lower, particle diameter to show also the effect of it on the profiles.
It is not possible to appreciate an evident difference between the two models that predict similar profiles in terms of phase fraction and velocity. The effect of the lower particle diameter is instead very clear: the smaller particles are more easily dragged by the carrier liquid resulting in a more homogeneously dispersed phase fraction profile related to a velocity profile that resembles the one of a pure liquid. Another effect to be highlighted due to the different particle size is an increase of the pressure drop, probably associated to the fact that in a control volume of the flow more particles can be contained leading to an higher frequency of collisions that in turn causes a loss of momentum and hence a higher pressure drop.

5.4.2 Comparison with experimental data

The next step was to compare the pressure drop and profiles against experimental data from [53]. Table 5.5 summarizes the parameters for the two models simulations.

Figure 5.8 shows the pressure profiles comparison against Syamlal and Gidaspow model. It's possibile to see how the prediction quality for high velocities is very good with the Gidaspow model while Syamlal model is overestimating pressure drop along all the velocity regimes. The bad prediction quality for lower velocities is possibly addressable to the fact that in those regimes most of the solid particulate is lying in a stationary bed on the bottom and the frictional stress is the leading process compared to the collisional component. The frictional model used is provided by Johnson and Jackson [44] (see Equation (3.49)), and it depends from several hand-picked parameters that could influence the resulting frictional stress.

For what concerns instead the phase fraction prediction quality, in Figure 5.9 is shown the comparison among the CFD models and experimental data for the conditions with $\alpha = 0.3, u = 3\,\mathrm{m/s}$. The phase fraction is normalized, since in [53] the graphs are given in normalized axis, to achieve the same value for $\frac{r}{D} = -0.5$.
The Gidaspow model, even for the phase fraction simulation, results in better agreement with respect to the Syamlal one. The deposition rate is higher for both numerical simulations, the particles are

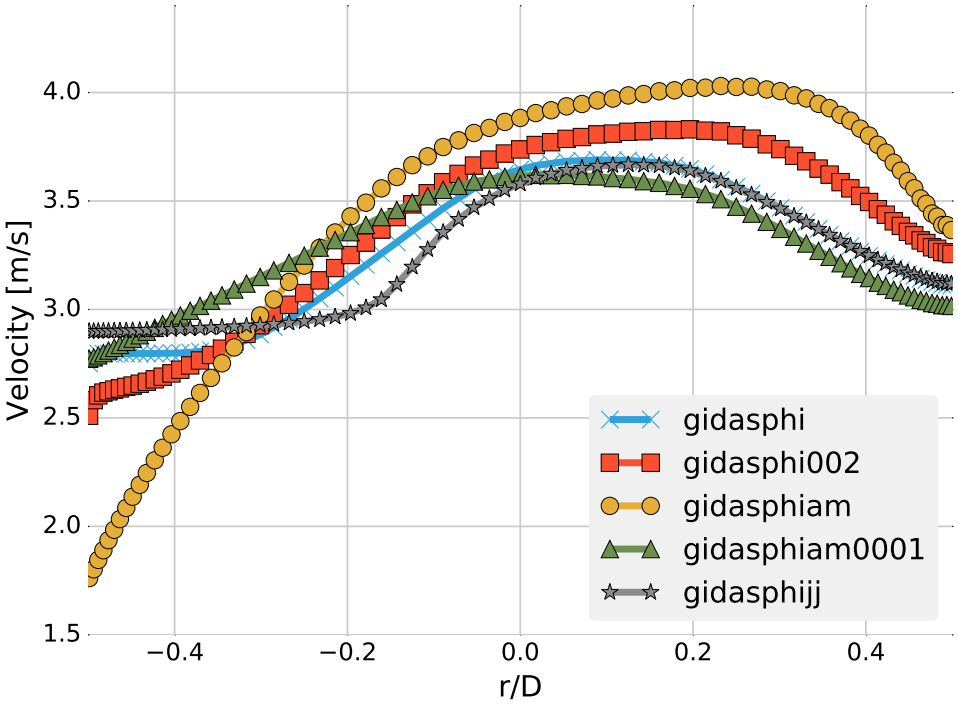

Figura 5.4: Velocity Profiles comparison for Gidaspow model

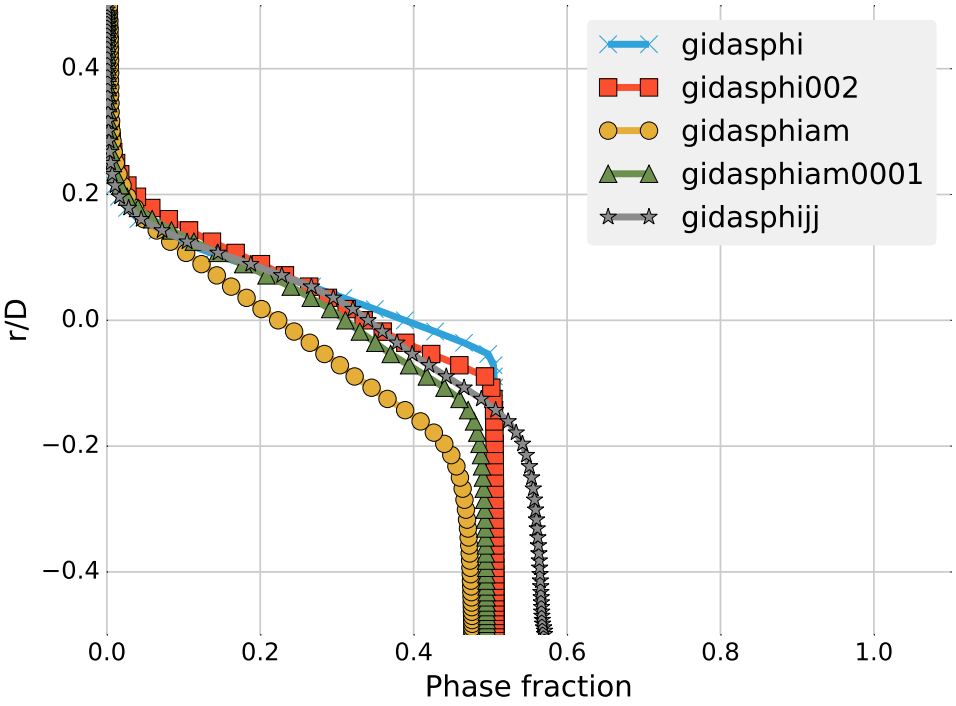

Figura 5.5: α Profiles comparison for Gidaspow model

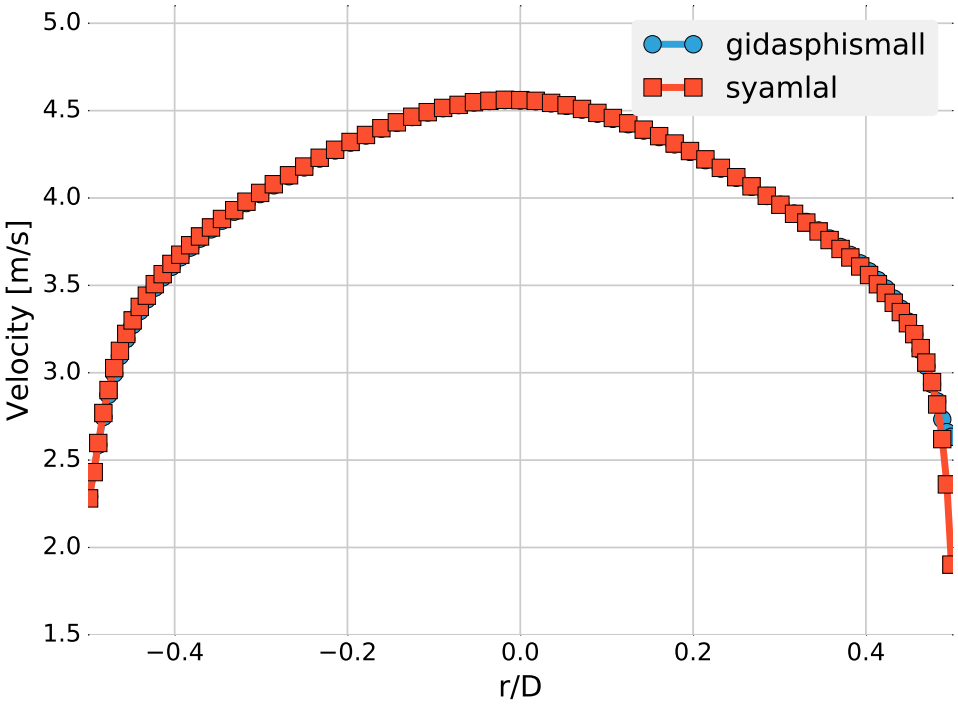

Figura 5.6: Gidaspow vs Syamlal velocity profiles comparison

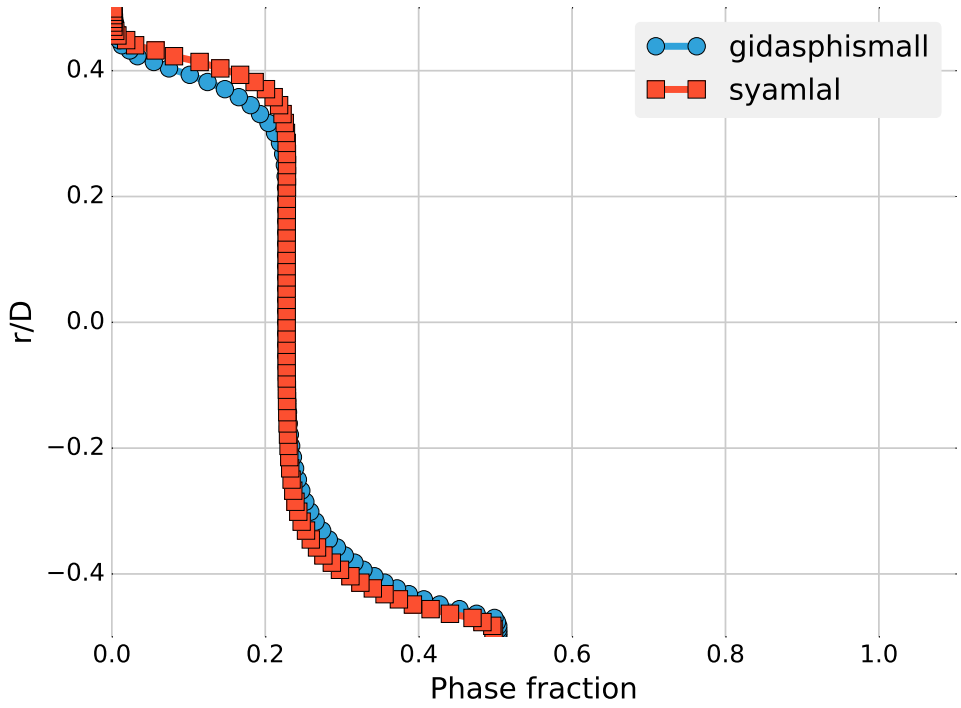

Figura 5.7: Gidaspow vs Syamlal α profiles comparison

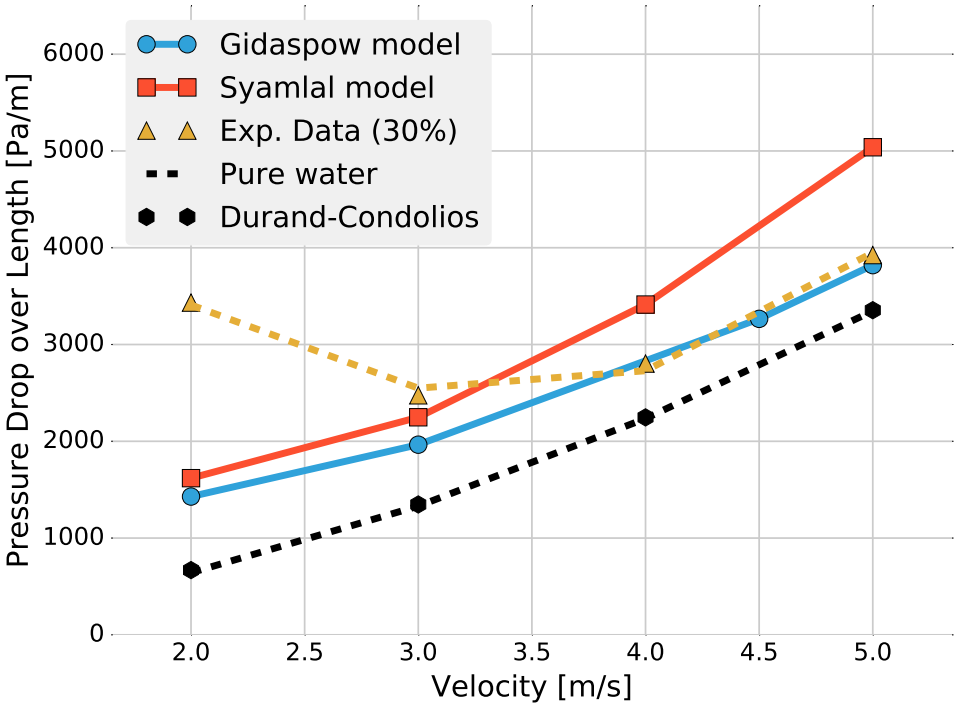

Figura 5.8: Pressure drop for Kaushal case

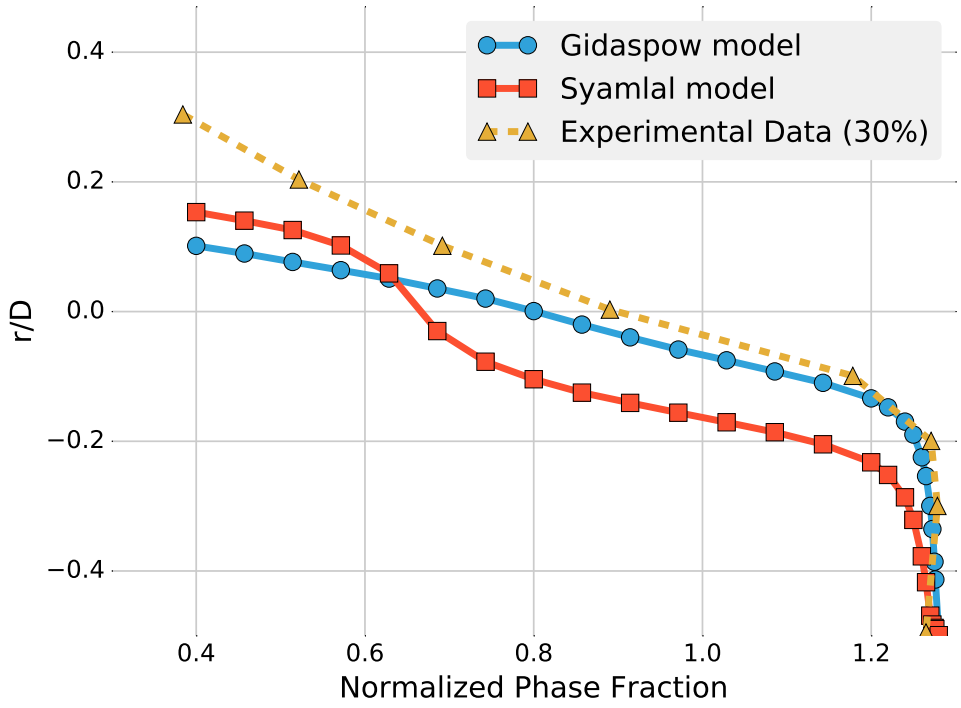

Figura 5.9: Phase fraction for Kaushal case

settling more than in the experimental case, the overall slope of the α profile is satisfying. All the results are summarized in Table 5.6.

5.5 SLN2 slush

The second case analyzed is a SLN2 slush case whose experimental data are provided by Ohira *et al* in [12], the thermo-physical properties of the slush are shown in Table 5.7 . In the case of the slush flow, the particle shape is not fully known since measuring it is difficult due to the very low temperature of the SLN2 together with the intrinsic heterogeneous nature of the solid particles that are solidified during the slush production process. The pressure drop comparison is reported in Figure 5.10 and summarized in Table 5.8.

As it is possible to see, the prediction of the pressure drop over the different flow velocities is in good agreement with the experimental data. The pressure-drop rise for low velocities experienced in the water-glass-beads case is not noticeable, one reason could be the different domain: the pipe has smaller diameter and length, the walls are closer and the collision of the particles keep the slush more homogeneous with less settling tendency.

In Figure 5.11 the profiles for the solid fraction are displayed. In that image is possible to see the effect of the increasing inlet velocity over the particle distribution along the diameter. The α value is normalized with the inlet value $\alpha/\alpha_{\text{inlet}}$.

Model	**Velocity** $\left[\frac{\text{m}}{\text{s}}\right]$	δ	α_{max}	e	e_w	ϕ	$\frac{\Delta p}{L}$
Gidaspow	1	28.5	0.5	0.9	0.9	0.001	880
Gidaspow	2	28.5	0.5	0.9	0.9	0.001	1429
Gidaspow	3	28.5	0.5	0.9	0.9	0.001	1965
Gidaspow	4.5	28.5	0.5	0.9	0.9	0.001	3265
Gidaspow	5	28.5	0.5	0.9	0.9	0.001	3821
Syamlal	1	28.5	0.5	0.9	0.9	0.01	775
Syamlal	2	28.5	0.5	0.9	0.9	0.01	1619
Syamlal	3	28.5	0.5	0.9	0.9	0.01	2248
Syamlal	4	28.5	0.5	0.9	0.9	0.01	3413
Syamlal	5	28.5	0.5	0.9	0.9	0.01	5038

Tabella 5.6: Kaushal case results summary

Pipe Diameter [mm]	**Liquid Viscosity** [Pa s]	**Solid Density** $\left[\frac{\text{kg}}{\text{m}^3}\right]$	**Liquid Density** $\left[\frac{\text{kg}}{\text{m}^3}\right]$
15	0.292e−3	1026.5	867.86

Tabella 5.7: Slush case properties

The effect of velocity follows the intuition that for higher flow rates particles are more strongly interacting with the carrier fluid leading to a way more homogeneous distribution along the diameter.

In Figure 5.12 it is possible to appreciate the influence of the concentration on the α profile. With the Gidaspow model for a slush flow with a 13% volume concentration of solid particles the particles are distributed less homogeneously than for the 30% case. This is linked to the fact that with a lower concentration the average rate of collision for particles is reduced, there is less fluctuation, the particles tend to settle more. No sensible differences between the two models are reported.

In Figure 5.13 a check on the prediction quality for the velocity profiles is plotted. Since in the original paper of the experimental data the values for the velocity are given normalized over an unknown mean velocity u/u_{mean}, the results of the CFD simulations are normalized in order to have same maximum value as the experimental outcomes. Moreover the CFD velocity plotted is a mixture velocity,

Model	**Velocity** $\left[\frac{\text{m}}{\text{s}}\right]$	δ	α_{max}	e	e_w	ϕ	$\frac{\Delta p}{L}$
Syamlal	1	28.5	0.5	0.9	0.9	0.01	1192
Syamlal	2	28.5	0.5	0.9	0.9	0.01	3059
Syamlal	3	28.5	0.5	0.9	0.9	0.01	5958
Syamlal	4	28.5	0.5	0.9	0.9	0.01	9715
Syamlal	5	28.5	0.5	0.9	0.9	0.01	14368
Gidaspow	2	28.5	0.5	0.9	0.9	0.01	2817
Gidaspow	3	28.5	0.5	0.9	0.9	0.01	5860
Gidaspow	4	28.5	0.5	0.9	0.9	0.01	9888
Gidaspow	5	28.5	0.5	0.9	0.9	0.01	14858

Tabella 5.8: Slush case results summary

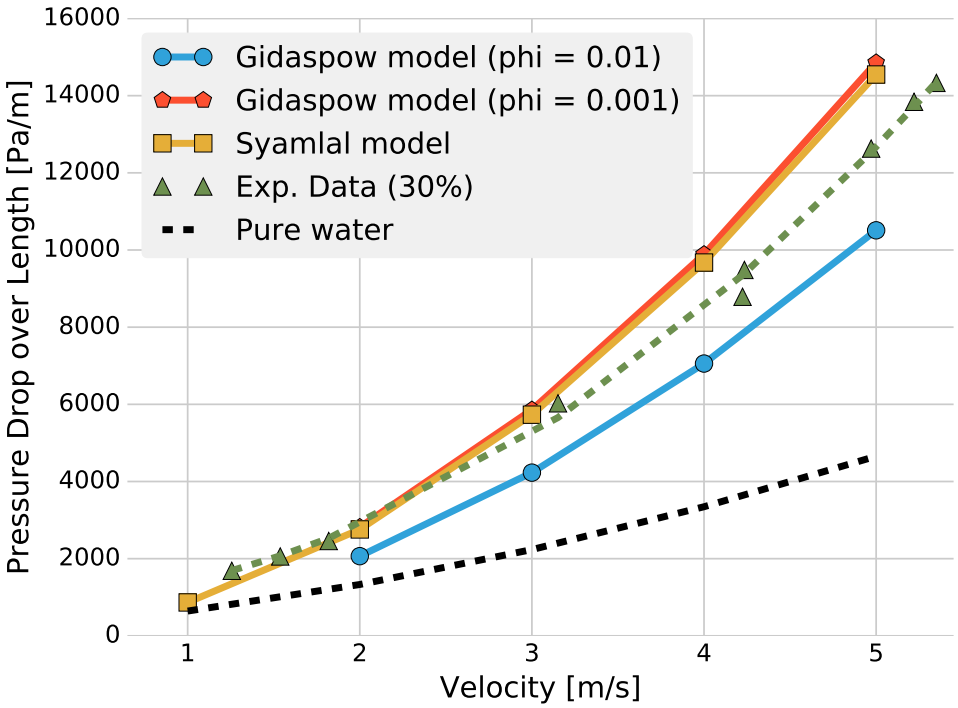

Figura 5.10: Pressure drop for slush case

expressed by Equation (5.3)

$$\mathbf{u} = \alpha \mathbf{u}_s + (1-\alpha)\,\mathbf{u}_{\text{liquid}} \tag{5.3}$$

The results are in good agreement with the experimental data, it is possible to record a small velocity leak in the upper part of the pipe ($r/D > 0.1$) that is caused by an higher deposition in the experimental case compared to the simulated one.

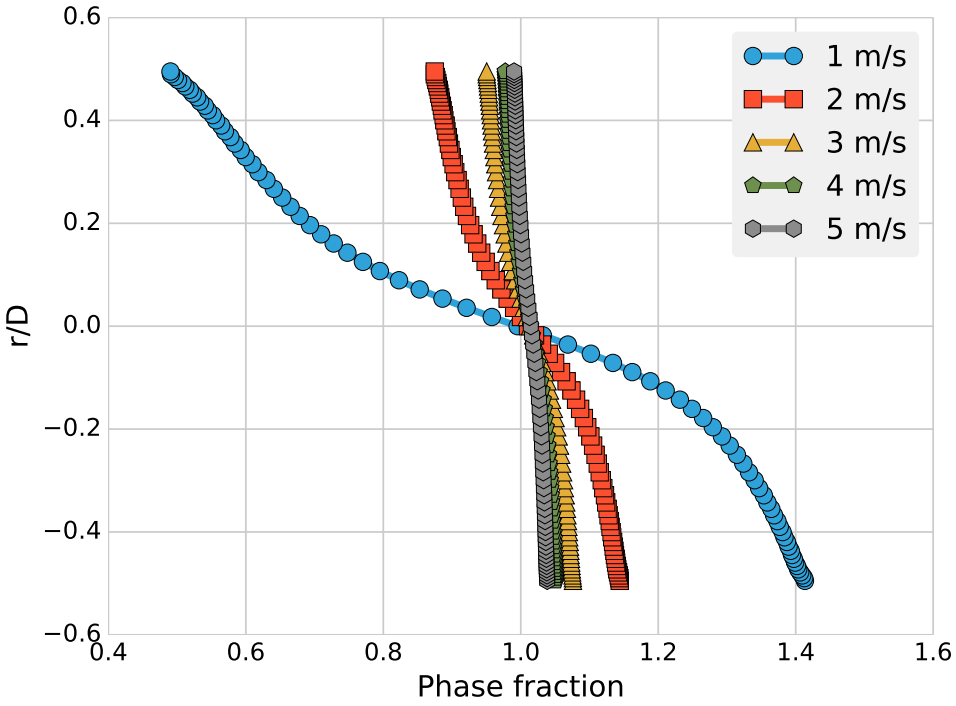

Figura 5.11: α profiles for slush case

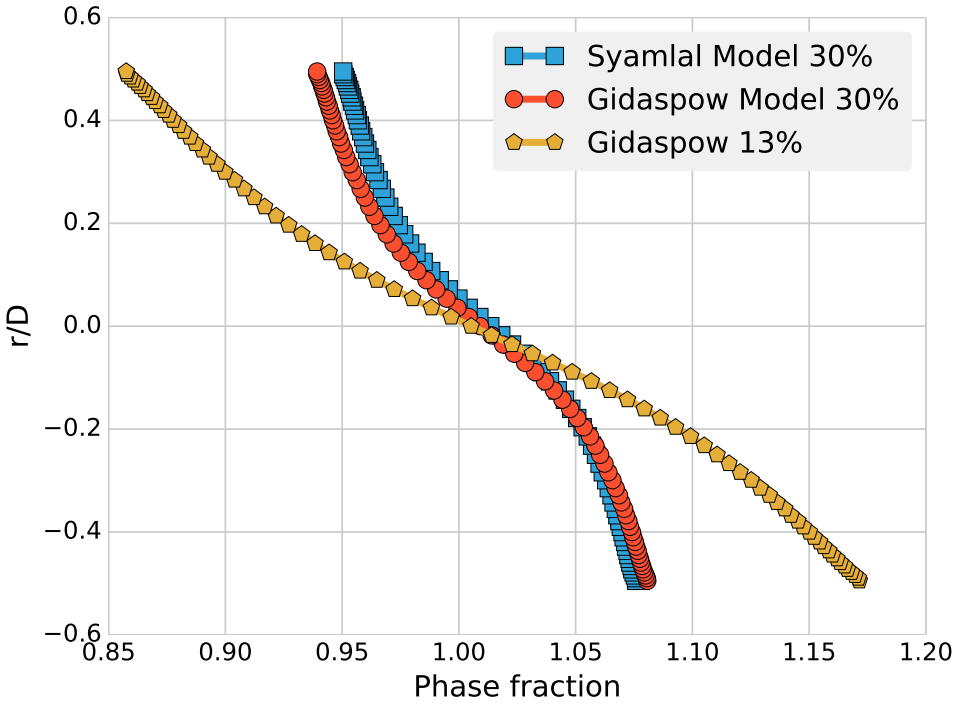

Figura 5.12: α profiles comparison. $u = 3.0$ [m/s]

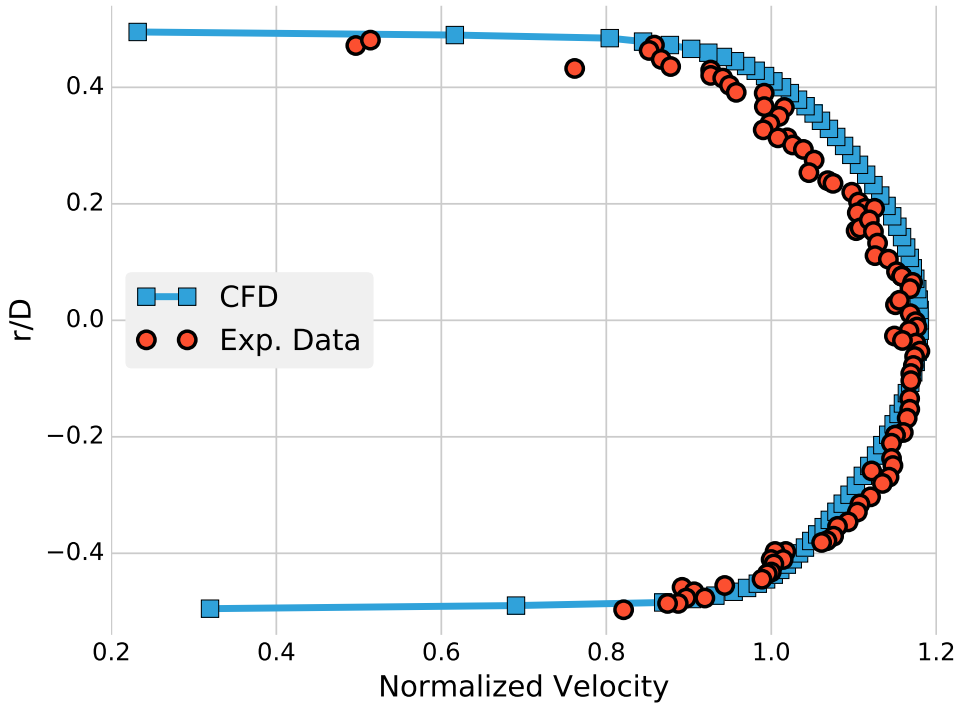

Figura 5.13: Velocity profile check against exp. data. $u = 2.0$ [m/s]

Capitolo 6

Conclusions

The importance of being able to simulate high-concentration slurries and slushes is of vital importance in order to achieve a better efficiency in the process of design and development of propulsion systems for the next generation launchers. In the present work the Euler-Euler model for the numerical computation of two-phase solid-liquid flows has been thoroughly investigated in terms of prediction capability for hydrodynamic (incompressible) properties. The results presented in Chapter 5 demonstrate how the Eulerian approach is a solid alternative to Euler-Lagrange for high and very high solid concentration (up to 30%), mainly because of the too intense computational cost connected to the lagrangian tracking of an high number of particles.
The quality of prediction for pressure drops is in good agreement with literature experimental data especially for high inlet velocities of the flow even if the correct value is strongly dependant on the choice of the KTGF parameters, mainly the specularity coefficient ϕ that has to be carefully handpicked to reach satisfying prediction quality. For lower velocities, in geometries with bigger diameters, the particles are settling on the bottom of the pipe creating a stationary bed that is mainly driven by frictional stress that is not fully reproduced, at least in the case analyzed, by the closure equations provided by the Kinetic Theory for granular flows.

Reasonable accuracy is also obtained for solid fraction profile over the pipe diameter, in particular for the Kaushal case, where the pipe diameter is not very small, the slope of the α profile is reproduced with very good agreement.

The velocity profile computed for the slush case and compared with Ohira experimental results is also in close agreement with the PIV outcomes of Ohira work.

OpenFOAM has demonstrated to be a good choice for the analysis of solid-liquid multiphase flows also thanks to its opensource nature that allows the decomposition of the case on several, arbitrarily numbered, computational units without any additional[1] cost.

6.0.1 Future Improvements

From the somehow preliminary results of this work several different paths for future improvements are possible, both in theoretical-numerical and experimental declinations.

[1] additional to the cost of hardware

Theoretical-Numerical

- The analysis performed does not account for thermal effects. The slush flows are promising applications of multiphase flows also because their possibility of undergoing phase change. The natural following extension to the present study is to account for heat and mass exchange in the numerical simulation. OpenFOAM is already equipped with a solver, `reactingEulerFoam`, that already implements several models for energy and mass transfer. It could be a good starting point for the future analysis.
- A pipe is only one of the several domains that are interesting for propulsion systems. The same analysis performed on other components like injectors, valves, angle-pipes, inclined-pipes would paint a more complete scenario of the capabilities of this modeling strategy applied to propulsion complex assemblies.
- A minor task that would really ease the current simulation status would be the redesign of the `yPlus` tool provided by OpenFOAM to compute turbulence wall Y^+ increasing its abstraction in order to allow the direct computation of Y^+ also for `twoPhaseEulerFoam` cases that is currently not possible.

Experimental

- At Von Karman Institute for Fluid Dynamics (VKI) a new experimental facility for the study of cryogenic LN2 and SLN2 is available. Following the path originated from this work we suggest to perform a broad experimental campaign to produce additional data to be cross-checked with the CFD setup here presented and to derive an as-general-as-possible experimental correlation.
- Literature is lacking a statistically-relevant number of experimental data about thermal properties of slush flows. Computing heat-exchange coefficient and solid-fraction loss due to thermal heat leak is incredibly important to achieve a complete awareness of the phenomenon.
- Aging of slushes is one of the main reasons that are still keeping the space industry from using them in space launchers. An experimental campaign addressed to the study of this problem would really improve the current knowledge of the physics of this kind of flows finally leading to the implementation of industry-ready propulsion systems based on slush fuel/oxidizers.

Acknowledgements

[2]

It is funny how you always believe to walk alone along the impervious road that leads to graduation but when you just stop, being almost at the end, few lines literally far from the end, you realize how many people you met that in a way or in another changed your life. As I always keep saying recently, it is not about the notions you learn, it is about the people you meet.

First of all, I would like to express my profound gratitude and love to my family. My dad, my mum, my brother. They kept supporting me along this difficult journey making me feel as the most beloved person in the world. They have been, and keep being, an example for me.

I would like to thank my supervisor Prof. Luciano Galfetti for supporting the incredible adventure in Skyward Experimental Rocketry and for allowing me to choose to develop this thesis abroad at VKI. An heartfelt thanks to Prof. Maria Rosaria Vetrano, co-supervisor at VKI for helping me to develop this work in the best way possible; I am very honored to have the possibility to continue the project in the next year at VKI. I would also like to thank Prof. Jean-Marie Buchlin for helping me to understand in more depth the subject involved in this thesis.

A piece of merit for the growth of a student surely goes to his teachers, I would like to thank Prof. Alessandro Giovannetti for teaching me to be a proud student, Prof. Rosella Valentini for the energy spent for culture, Prof. Filomena Cipriani for enlightening my mind with her unstoppable enthusiasm and contagious love and passion for Mathematics and Physics.
I would also like to thank Prof. Quartapelle, undoubtedly the professor I learnt more from at PoliMI, for the countless pills of wisdom about life and Fluid Dynamics. Thanks to Prof. Topputo and Prof. Di Lizia, for the competence and passion - a rare good among PoliMI professors - that inspired me during these years.

I would also like to mention Skyward Experimental Rocketry friends and colleagues, we achieved amazing heights and it was an honor to share that experience with you all. A special thanks goes to Michele, Giovanni and Jonata, for being such a pushing force. I'm sure you will revolutionize the world. Thanks for involving me in your projects.
Being the best I could would have been hard without the amazing *stagiaires* at VKI. Sharing the same room with you was one of the most stimulating experience of my life. Thanks for being the best you can to Max, Ed, Pacome, Fran, Rahand, Nishant and all the others. I would also like to acknowledge Maria for being a precious help while fighting with OpenFOAM. Thanks to Simon for being an invaluable source of optimism, I'm very happy to share another (probably rainy) year in Belgium with you. Audrey, for all the useful comments and opinions about my work and my projects.

[2]This work was financially supported by Politecnico di Milano (PoliMI)'s *Tesi all'estero* scholarship.

It is always easier to climb a mountain if you have expert mountain guides at your side, friends like Lorenzo e Michele are the fuel of my ambitions. I am proud and honored to have such an example of dedication, competence and optimism in my life. From the first day we met at Princeton you inspired me to be the best I could. Thanks for the countless all-night-long stimulating conversations, for the appreciated visit in Belgium and for being amazing like you are.

Thanks to Luca Di Pancrazio, for sharing with me life, dreams and pains of studying here in Milan. It is hard to face a person like me, thanks for being a true friend.

Thanks to Riccardo, the most skillful engineer I know, for the lots of discussions we had about everything. I would without hesitation bet my life on his competence.

Thanks to Luigi, for being my desk mate at school (of life).

Thanks to Matteo, for the shared love for dachshunds and the solid lasting friendship.

A special mention goes to Jon. We always had a strong link between our souls that made us more than friends. Thanks for being in my life since the beginning. I love you like a brother.

Thanks, last but surely not least, to Federica. You colored my life here with peace and love. Thanks for being on my side.

Thanks to all the amazing people I met. You changed my life.

Appendices

Appendice A

`pyslurry` User Guide

For the cross-check of the CFD and experimental data of the cases analyzed in this work, several correlations have been tested and the most useful one are also briefly described in Chapter 4. Since correlations are very handy to preliminary state the correctness of a simulation or of an experimental test, a framework developed to account for an easy-to-implement tool for slurry and slush correlations has been started.

`pyslurry` is a Python library programmed with an object-oriented philosophy aimed to possibly collect all the useful correlations for slurry and slush flows. It is coded using `numpy` and `scipy` numerical modules for Python and it is very easy to use. In Listing A.1 it is shown how to estimate pressure drops for a slurry and a slush flow in the same pipe.

Listing A.1: example code

```
from pyslurry.fluid import SlurryWater
from pyslurry.fluid import SlushNitrogen
from pyslurry.pipeflow import HorizontalPipe
from pyslurry.pipeflow.models import DurandCondoliosGibert, Turbulent

slurry = SlurryWater(C=0.3, rho_s=2470, d=1E-3)
sln2 = SlushNitrogen(C=0.3, d=1E-3)

pipe = HorizontalPipe(D=55E-3, L=3, U=3)

slurry_case = DurandCondoliosGibert(slurry, pipe)
slush_case = DurandCondoliosGibert(sln2, pipe)

pure_water = Turbulent(slurry, pipe)
pure_ln2 = Turbulent(sln2, pipe)

print(slurry_case.dp(), slush_case.dp(), pure_water.dp(), pure_ln2.dp())
```

It is good to notice how just declaring a `SlurryWater` object we are creating a slurry that has water as liquid carrier. We still need to specify concentration `C`, particle diameter `d`, and solid particle density `rho_s`. In the `SlushNitrogen` case instead, we just had to specify concentration and particle diameter since the solid density is already known by the object itself.

All the fluid classes are stored in `pyslurry.fluid` module. It is obviously still possible to declare custom slurries:

Listing A.2: Custom declaration

```
from pyslurry.fluid import Slurry

custom_slurry = Slurry(rho = fluid_rho, rho_s = solid_rho,
                       C=concentration, mu = liquid_viscosity,
                       d=particle_diameter)
```

The module is currently an alpha version, models for Laminar (`Poiseuille`),Turbulent (`Turbulent`) pure fluid and non-developed laminar pure fluid (`NonDevPoiseuille`) are provided together with Durand and Condolios [49] (`DurandCondoliosGibert`), see Section 4.2, and Yuan and Turian [54], [55] (`TurianYuan1977`), see Section 4.3, correlations for solid-liquid multiphase flows.

The code will be released soon under a Free and Open Source Software (FOSS) license. Check my github profile for updates github.com/rubendibattista.

Acronimi

2FM Two-fluids model. 7, 27

AR Aspect Ratio. 7, 49

BC Boundary Condition. 3, 5, 7, 40, 41, 51, 52

CFCs Chlorofluorocarbons. 7, 13

CFD Computational Fluid Dynamics. 7, 27, 56, 63, 70, 75

DNS Direct Navier-Stokes Simulation. 7, 41

DPE Discrete Particle Element. 7, 33

E-E Euler-Euler. 7, 28

E-L Euler-Lagrange. 7, 28

ESA European Space Agency. 7, 9, 11, 13, 19

F-T Freeze-thaw. 7, 19, 21

FDM Finite Difference Method. 7, 28

FESTIP Future European Space Transportation Investigations Programme. 7, 9, 11, 13, 19

FLUSH FLow of slUSH. 7, 43, 45

FOSS Free and Open Source Software. 7, 76

FVM Finite Volume Method. 7, 28

GNU GNU's not Unix. 7

HRE Hybrid Rocket Engine. 7, 14

JAXA Japan Aerospace eXploration Agency. 7, 9, 11, 13

KTGF Kinetic Theory for granular flows. 7, 27, 28, 35, 49, 54, 69, 79

LH2 Liquid Hydrogen. 7, 13, 20, 23, 24, 44

LHS Left Hand Side. 7, 40

LN2 Liquid Nitrogen. 7, 13, 23, 24, 70

LOX Liquid Oxygen. 7, 13

LRE Liquid Rocket Engine. 7, 14

MULES MUlti-dimensionsal Limiter for Explicit Solution. 7, 49

N-S Navier-Stokes. 7, 28, 29

NASA National Aeronautics and Space Administration. 7, 9, 11, 43

NASP National Space Plane. 7, 9, 11, 13, 19, 43

NBPH2 Normal-Boiling-Point Hydrogen. 7

NIST National Institute of Standards and Technology. 7, 45

OpenFOAM Open source Field Operation And Manipulation. 7, 35, 49, 51, 52, 54, 69–71

PIV Particle Image Velocimetry. 7, 42, 69

PoliMI Politecnico di Milano. 7, 71

RANS Reynolds-Averaged Navier-Stokes equations. 7

RHS Right Hand Side. 7, 29, 31

SLH2 Slush Hydrogen. 5, 7, 9, 13, 19–25, 28, 43–45

SLH2O Slurry Ice. 7, 19

SLN2 Slush Nitrogen. 7, 19, 22–24, 28, 49, 62, 70

SLO2 Slush Oxygen. 7, 14, 19, 20

SRM Solid Rocket Motor. 7, 14

TP Triple-point. 7, 19, 44

TPH2 Triple-Point Hydrogen. 7

VKI Von Karman Institute for Fluid Dynamics. 7, 70, 71

Latin Symbols

$\mathbf{c}$	Particle fluctuating velocity in KTGF
C_D	Drag coefficient
C_L	Lift coefficient
$C_{\text{v.m.}}$	Virtual Mass coefficient
d_p	Diameter of a particle
e	Coefficient of restitution
e_w	Wall Coefficient of restitution
g	Gravity field at sea level $\left(9.81\left[\frac{\text{N}}{\text{Kg}}\right]\right)$
g_0	Radial distribution function
h	Enthalpy per unit of mass
P_f	Granular pressure additional term due to frictional stress
k	Turbulent kinetic energy
ℓ	Reference Length
$\overline{\mathbf{M}}_\varphi$	Phase momentum exchange term
p	Pressure
P_s	Granular pressure
$\overline{\mathbf{R}}$	Reynols stress tensor
$\mathbf{u}$	Velocity vector
$\mathbf{u}_r$	Relative velocity between particle and carrier
V	Volume
$\mathbf{v}_i$	Velocity of the interface between phases
V_p	Volume of a particle
v_t	Terminal settling velocity of a particle

$\mathbf{x}$	Position vector
Y_φ	Phase φ mass fraction

Greek Symbols

α_φ	Phase φ fraction
χ_φ	Phase indicator function
δ	Angle of friction
ϵ	Turbulent dissipation rate
γ	Generic property subjected to operators
κ_Θ	Granular conductivity
λ_s	Bulk viscosity of the granular phase
μ	Viscosity
μ_c	Carrier liquid viscosity
μ_f	Granular viscosity additional term due to frictional stress
μ_t	Turbulent viscosity
ω	Turbulent specific dissipation
ϕ	Specularity coefficient
ρ	Density
Σ	Surface Area per unit volume
Θ	Granular temperature

Non-dimensional Groups

Fr_{fl}	Flow Froude number sort
Fr_p	Particle Froude number sort
Co	Courant number $\frac{\lvert\mathbf{u}\rvert\Delta t}{\Delta x}$
Re_p	Particle Reynolds number $\frac{\rho\lvert\mathbf{u}_r\rvert D}{\mu_c}$
Re	Reynolds number $\frac{\rho UD}{\mu}$
St	Stokes number $\frac{18\mu_c}{\rho_p d_p^2}\frac{U}{D}$

Bibliografia

[1] C. Sindt, «A summary of the characterization study of slush hydrogen», *Cryogenics*, vol. 10, n. 5, pp. 372–380, 1970.

[2] C. F. Sindt, «Heat transfer to slush hydrogen», in *Advances in Cryogenic Engineering*, ser. Advances in Cryogenic Engineering 19, K. D. Timmerhaus, cur., DOI: 10.1007/978-1-4613-9847-9_52, Springer US, 1995, pp. 427–436, ISBN: 978-1-4613-9849-3 978-1-4613-9847-9.

[3] D. B. Mann, P. R. Ludtke, C. F. Sindt e D. B. Chelton, «Liquid-solid mixtures of hydrogen near the triple point», in *Advances in Cryogenic Engineering*, Springer, 1966, pp. 207–217.

[4] C. F. Sindt, P. R. Ludtke e D. E. Daney, *Slush hydrogen fluid characterization and instrumentation*. for sale by the Supt. of Docs., US Govt. Print. Off., 1969, vol. 377.

[5] D. E. Daney, P. R. Ludtke e C. F. Sindt, «Slush hydrogen pumping characteristics using a centrifugal-type pump», in *Advances in Cryogenic Engineering*, Springer, 1969, pp. 438–445.

[6] A. Friedlander, R. Zubrin e T. L. Hardy, «Benefits of slush hydrogen for space missions», 1 ott. 1991.

[7] S. Zhang. (2 mar. 2016). SpaceX keeps aborting liftoffs because rocket fuel is tricky, WIRED, indirizzo: http://www.wired.com/2016/03/spacex-keeps-aborting-liftoffs-rocket-fuel-tricky/ (visitato il 03/08/2016).

[8] M. A. Karabeyoglu, B. J. Cantwell e D. Altman, «Development and testing of paraffin-based hybrid rocket fuels», *AIAA paper*, vol. 4503, p. 2001, 2001.

[9] C. T. Crowe, cur., *Multiphase flow handbook*, ser. Mechanical engineering series, Boca Raton, Fla.: Taylor & Francis, 2006, ISBN: 978-0-8493-1280-9.

[10] Y. M. Park, «Literature research on the production, loading, flow, and heat transfer of slush hydrogen», *International Journal of Hydrogen Energy*, Asian Hydrogen Energy Conference 2009, vol. 35, n. 23, pp. 12 993–13 003, dic. 2010, ISSN: 0360-3199.

[11] S. Gürsu, S. A. Sheriff, T. N. Vezirocğlu e J. W. Sheffield, «Review of slush hydrogen production and utilization technologies», *International Journal of Hydrogen Energy*, vol. 19, n. 6, pp. 491–496, giu. 1994, ISSN: 0360-3199.

[12] K. Ohira, «Pressure drop reduction phenomenon of slush nitrogen flow in a horizontal pipe», *Cryogenics*, vol. 51, n. 7, pp. 389–396, lug. 2011, ISSN: 0011-2275.

[13] K. Ohira, S. Matsuo e H. Furumoto, «An experimental investigation of production and density measurement of slush hydrogen», *Cryogenics*, Fifteenth International Cryogenic Engineering Conference, vol. 34, Supplement 1, pp. 397–400, 1994, ISSN: 0011-2275.

[14] H. Fujiwara, M. Yatabe, H. Tamura, M. Takahashi, J. Miyazaki e Y. Tsuruta, «Experiment on slush hydrogen production with the auger method», *International Journal of Hydrogen Energy*, vol. 23, n. 5, pp. 333–338, mag. 1998, ISSN: 0360-3199.

[15] R. O. Voth, «Producing liquid-solid mixtures (slushes) of oxygen or hydrogen using an auger», *Cryogenics*, vol. 25, n. 9, pp. 511–517, 1 set. 1985, ISSN: 0011-2275.

[16] M. J. Baker, T. T. Denton e C. Herr, «An explanation for why it is difficult to form slush nitrogen from liquid nitrogen used previously for this purpose», *Cryobiology*, vol. 66, n. 1, pp. 43–46, feb. 2013, ISSN: 0011-2240.

[17] «Apparatus for making hydrogen slush using nitrogen and helium refrigerants», US3521457 A, U.S. Classification 62/54.1, 62/354, 62/467; International Classification F25J1/00; Cooperative Classification F25J1/0072, F25J1/0052, F25J1/001, F25J2210/42, F25J2290/42, F25J1/0221, F25J1/0065, F25J1/0205, F25J2205/20, F25J1/0276; European Classification F25J1/02, F25J1/02B4, F25J1/00R4N, F25J1/00C4V, F25J1/02F, F25J1/02Z4U2, F25J1/00R2H, F25J1/00A2W, 21 lug. 1970.

[18] N. B. Mcnelis, T. L. Hardy, M. V. Whalen, M. T. Kudlac, M. E. Moran, T. M. Tomsik e M. S. Haberbusch, «A summary of the slush hydrogen technology program for the national aero-space plane», **presentedat**Hypersonics Technologies Conference, Chattanooga, TN, United States, 1 apr. 1995.

[19] K. Ohira, K. Nakamichi e Y. Kihara, «Development of a waveguide-type flowmeter using a microwave method for slush hydrogen», *JSME International Journal Series B Fluids and Thermal Engineering*, vol. 48, n. 1, pp. 114–121, 2005.

[20] K. Ohira, «Study of nucleate boiling heat transfer to slush hydrogen and slush nitrogen», *Heat Transfer—Asian Research*, vol. 32, n. 1, pp. 13–28, 1 gen. 2003, ISSN: 1523-1496.

[21] Y. Jiang e P. Zhang, «Pressure drop and flow pattern of slush nitrogen in a horizontal pipe», *AICHE Journal*, vol. 59, n. 5, pp. 1762–1773, mag. 2013, ISSN: 00011541.
[22] A. Carapelle e J. .-.-P. Collette, «Gamma-ray attenuation for measuring cryogenic slush mixture density», *Nuclear Instruments and Methods in Physics Research Section B: Beam Interactions with Materials and Atoms*, vol. 229, n. 1, pp. 111–116, feb. 2005, ISSN: 0168-583X.
[23] N. US Department of Commerce. (). NIST XCOM: Photon cross sections database, indirizzo: http://www.nist.gov/pml/data/xcom/ (visitato il 19/02/2016).
[24] K. Ohira, «Development of density and mass flow rate measurement technologies for slush hydrogen», *Cryogenics*, vol. 44, n. 1, pp. 59–68, gen. 2004, ISSN: 0011-2275.
[25] K. Ohira, A. Ota, Y. Mukai e T. Hosono, «Numerical study of flow and heat-transfer characteristics of cryogenic slush fluid in a horizontal circular pipe (SLUSH-3d)», *Cryogenics*, vol. 52, n. 7, pp. 428–440, lug. 2012, ISSN: 0011-2275.
[26] K. Ohira, K. Nakagomi e N. Takahashi, «Pressure-drop reduction and heat-transfer deterioration of slush nitrogen in horizontal pipe flow», *Cryogenics*, vol. 51, n. 10, pp. 563–574, ott. 2011, ISSN: 0011-2275.
[27] R. S. Collier, «Thermally induced oscillations in cryogenic systems», 1972.
[28] T. E. Rhafiki, «Modélisation et étude numérique d'un écoulement diphasique solide-liquide subissant un chagement de phase dans un échangeur de chaleur. application aux coulis de glace et stabilisé», tesi di dott., Université de Pau et des Pays de l'Adour Pau-France, dic. 2009.
[29] Y. Jiang e P. Zhang, «Numerical investigation of slush nitrogen flow in a horizontal pipe», *Chemical Engineering Science*, vol. 73, pp. 169–180, mag. 2012, ISSN: 00092509.
[30] J. Ishimoto e R. Ono, «Numerical study of the two-phase flow characteristics of slush nitrogen», *Cryogenics*, vol. 45, n. 4, pp. 304–316, apr. 2005, ISSN: 0011-2275.
[31] L. Chen, Y. Duan, W. Pu e C. Zhao, «CFD simulation of coal-water slurry flowing in horizontal pipelines», *Korean Journal of Chemical Engineering*, vol. 26, n. 4, pp. 1144–1154, lug. 2009, ISSN: 0256-1115, 1975-7220.
[32] D. Kaushal, T. Thinglas, Y. Tomita, S. Kuchii e H. Tsukamoto, «CFD modeling for pipeline flow of fine particles at high concentration», *International Journal of Multiphase Flow*, vol. 43, pp. 85–100, lug. 2012, ISSN: 03019322.
[33] J. Wang, T. Zhang e S. Wang, «Heterogeneous ice slurry flow and concentration distribution in horizontal pipes», *International Journal of Heat and Fluid Flow*, vol. 44, pp. 425–434, dic. 2013, ISSN: 0142-727X.
[34] D. P. Hill, «The computer simulation of dispersed two-phase flow», tesi di dott., University of London, 1998.
[35] P. Crivellari, L. del Monte e F. Gamma, «Computational fluidynamics of hydrogen for aerospace vehicles», 1999.
[36] F. Gamma, L. del Monte e R. Liberatore, «CFD-analysis of slush hydrogen flows in feed-systems of rocket-based combined cycles», in *AIAA/ASME/SAE/ASEE Joint Propulsion Conference & Exhibit, 34 th, Cleveland, OH*, 1998.
[37] P. Reynier, M. Bugel e J. Lecoîntre, «Review of the modelling of slush hydrogen flows», *The Journal of Computational Multiphase Flows*, vol. 3, n. 3, pp. 123–146, 1 set. 2011, ISSN: 1757-482X.
[38] H. Rusche, «Computational fluid dynamics of dispersed two-phase flows at high phase fractions», tesi di dott., Imperial College London (University of London), 2003.
[39] C. Dopazo, «On conditioned averages for intermittent turbulent flows», *Journal of Fluid Mechanics*, vol. 81, n. 3, pp. 433–438, 1977.
[40] A. D. Gosman, C. Lekakou, S. Politis, R. I. Issa e M. K. Looney, «Multidimensional modeling of turbulent two-phase flows in stirred vessels», *AICHE Journal*, vol. 38, n. 12, pp. 1946–1956, 1992.
[41] B. G. M. v. Wachem, «Derivation, implementation, and validation of computer simulation models for gas-solid fluidized beds», *ResearchGate*,
[42] J. Lundberg e B. M. Halvorsen, «A review of some exsisting drag models describing the interaction between phases in a bubbling fluidized bed».
[43] D. Gidaspow, *Multiphase flow and fluidization: Continuum and kinetic theory descriptions*. Boston: Acad. Press [u.a.], 1994, 467 pp., ISBN: 978-0-12-282470-8.
[44] P. C. Johnson e R. Jackson, «Frictional–collisional constitutive relations for granular materials, with application to plane shearing», *Journal of Fluid Mechanics*, vol. 176, pp. 67–93, 1987.
[45] D. G. Schaeffer, «Instability in the evolution equations describing incompressible granular flow», *Journal of differential equations*, vol. 66, n. 1, pp. 19–50, 1987.
[46] S. A. Miedema, «An overview of theories describing head losses in slurry transport: A tribute to some of the early researchers», in *ASME 2013 32nd International Conference on Ocean, Offshore and Arctic Engineering*, American Society of Mechanical Engineers, 2013, V04AT04A038–V04AT04A038.
[47] T. L. Hardy, «Flush: A tool for the design of slush hydrogen flow systems», 1 feb. 1990.
[48] J. R. Fowler e R. C. Hendricks, «Computing properties of pure and mixed fluids», 1993.
[49] R. Durand e E. Condolios, «Experimental investigation of the transport of solids in pipes», *Deuxieme Journée de lhydraulique, Societé Hydrotechnique de France*, 1952.
[50] S. Sadat-Helbar, E. Amiri-Tolkadany, Steve Darby e A. Shafaie, «Fall velocity of sediment particles»,
[51] R. M. Turian e T.-F. Yuan, «Flow of slurries in pipelines», *AICHE Journal*, vol. 23, n. 3, pp. 232–243, 1 mag. 1977, ISSN: 1547-5905.
[52] R. M. Turian, F.-L. Hsu e T.-W. Ma, «Estimation of the critical velocity in pipeline flow of slurries», *Powder Technology*, vol. 51, n. 1, pp. 35–47, 1987.

[53] D. Kaushal, K. Sato, T. Toyota, K. Funatsu e Y. Tomita, «Effect of particle size distribution on pressure drop and concentration profile in pipeline flow of highly concentrated slurry», *International Journal of Multiphase Flow*, vol. 31, n. 7, pp. 809–823, lug. 2005, ISSN: 03019322.

[54] R. M. Turian, F. L. Hsu e M. S. Selim, «FRICTION LOSSES FOR FLOW OF SLURRIES IN PIPELINE BENDS, FITTINGS, AND VALVES», *Particulate Science and Technology*, vol. 1, n. 4, pp. 365–392, ott. 1983, ISSN: 0272-6351, 1548-0046.

[55] R. M. Turian, T.-F. Yuan e G. Mauri, «Pressure drop correlation for pipeline flow of solid-liquid suspensions», *AICHE Journal*, vol. 17, n. 4, pp. 809–817, 1 lug. 1971, ISSN: 1547-5905.